PEER REVIEWED

Development of Solution Precursor Plasma Spray (SPPS) Yttrium Aluminum Garnet (YAG) Coatings for Engine Components Using a High Enthalpy Cascaded Arc Gun: Part I

Rishi Kumar[1] · Chen Jiang[1] · Brent Cottom[2] · Maurice Gell[1] · Eric H. Jordan[1]

Abstract Solution precursor plasma-sprayed (SPPS) yttrium aluminum garnet (YAG) thermal barrier coatings (TBCs) have previously been shown to have higher temperature capability and reduced thermal conductivity compared to state-of-the- art TBCs. This previous work was conducted using a relatively low enthalpy plasma gun (Metco 9 MB) and TBCs were deposited on laboratory specimens. The primary goal of this work was to advance the state of technology readiness of SPPS YAG TBC coatings by using a high enthalpy cascaded arc gun (Sinplex Pro) to produce varied microstructures optimized for specific engine components: a fuel nozzle tip, an annular combustor liner, and turbine ceramic outer air seals. The microstructure and properties of these TBCs have been characterized and shown to be superior to those obtained previously. Based on these favorable results, the processing technology was transferred to solar turbines incorporated. Their process optimization of coatings for the three engine components and the rig and engine testing of the coated components will be described in Part II of this paper.

✉ Rishi Kumar
  rkumar@solutionspray.com

1 Solutions Spray Technologies LLC, 270 Middle Turnpike, Storrs, CT 06269, USA

2 Solar Turbines Incorporated, 4200 Ruffin Rd, San Diego, CA 92123, USA

Introduction

Thermal barrier coatings (TBCs) are ceramic coatings employed in gas turbine engines for thermal protection of metallic components, thereby allowing the gas turbines to operate at higher temperatures to enhance efficiency (Ref 1-4). Since the efficiency of the gas turbine increases with operating temperature, there is a need to increase the temperature by using more effective component cooling systems and higher temperature TBCs (Ref 5, 6). The most commonly used TBC material to date is 6-8 wt.% yttria stabilized zirconia (YSZ) (Ref 1) because it reliably provides desired thermal and mechanical properties including: high fracture toughness for cyclic performance (Ref 7), a high coefficient of thermal expansion (CTE) (Ref 8) that minimizes the stress generated due to expansion mismatch with the underlying metallic substrate (Ref 1), and low thermal conductivity to provide a steep temperature gradient. However, with increasing operating temperatures (> 1200 °C), YSZ starts to undergo a martensitic phase transformation from the metastable tetragonal phase to the cubic and monoclinic phases, accompanied by volumetric change that causes premature spallation and fracture in the coating (Ref 9, 10). This issue is compounded at temperature exceeding 1200 °C when silicate deposits (calcium-magnesium- alumino-silicate or CMAS, volcanic ash and fly ash) start to melt and attack YSZ mechanically and chemically (Ref 11, 12). The silicate melt infiltrates the pores of the TBCs and compromise strain tolerance while simultaneously reacting with YSZ to form undesirable phases.

As a result, several different materials have been studied as a potential replacement for YSZ (Ref 5, 8, 13-16) (e.g., modified YSZ compositions (Ref 3, 17-20), perovskites

(Ref 21, 22), garnets (Ref 23-27) and zirconates (Ref 28-31).

In this work we have developed yttrium aluminum garnet (YAG-Y3Al5O12) TBCs using the solution precursor plasma spray (SPPS) process (Ref 32-36) and employed a cascaded arc plasma gun, Metco Sinplex Pro. A schematic of the SPPS process is shown in Fig. 1. The motivation for the choice of coating process (SPPS) and the TBC material (YAG) has been extensively studied and published, where it was demonstrated that SPPS YAG coatings have superior properties (critical to TBCs) as compared to APS 7YSZ in laboratory tests. These properties include lower thermal conductivity (0.58 W/mK at 1300 °C (Ref 26, 27), higher sintering resistance, longer cyclic durability, enhanced erosion resistance (Ref 23). YAG was also demonstrated to have phase stability up to 1600 °C and better CMAS performance as compared to YSZ (Ref 24). Using the SPPS process the microstructure of YAG coatings can be engineered to produce different intensities of horizontal porosities called inter-pass boundariers (IPBs) which were shown to reduce thermal conductivity and increase CMAS resistance of coating by laterally spreading the CMAS melt in the IPBs and reducing the vertical infiltration of CMAS in the coatings (Ref 26, 27, 31, 37). Table 1 summarizes the properties of SPPS YAG and APS YSZ coatings that were generated in the previous studies.

The aforementioned work on SPPS YAG (Ref 23, 24, 26, 27) was deposited by the Metco 9 MB plasma gun using a BETE pressurized gas atomizing precursor injection system. In the current study, the Metco SinplexPro plasma gun is used instead with either of two non-atomizing nozzles, a cylindrical stream injection and a fan injector. Different injectors were used to achieve the different microstructural goals for different engine components. The 9 MB plasma gun is known to have temperature and energy fluctuations in the plasma jet because of the complex interdependence of the process gases and plasma arc (Ref 38). The lower maximum energy allowed in 9 MB gun also limits the maximum feed rate of precursor and the ultimate deposition rate, as higher feed rate values result in a higher fraction of the precursor reaching the substrates in the un-pyrolyzed form, thereby creating soft and porous coatings. The problem can be mitigated using a cascaded arc gun (Metco Sinplex Pro) featuring a constrained arc path (Ref 38, 39) which is more stable and efficient in converting electric power to jet enthalpy. This requires higher voltages and significantly lower voltage instabilities, which should result in higher deposition efficiencies (Ref 40). This gun also can run at a higher overall power level with higher efficiency of converting electrical power to jet enthalpy leading to the ability to handle higher precursor feed rates and an increase in standoff distance.

In running systematic Taguchi experiments two levels of each parameter need to be chosen. Preliminary experiments were run guided by our experience with this process to choose appropriate parameter ranges to avoid parameter choices that produce very poor coatings or even no coating at all. Later a systematic approach is employed to generate a variety of microstructures that are property specific, like a porous microstructure with high density of IPBs for extremely low thermal conductivity and a highly dense coating for enhanced erosion resistance.

Fig. 1 A schematic of the SPPS process with the progressive physiochemical change of the precursor into a coating shown across the bottom
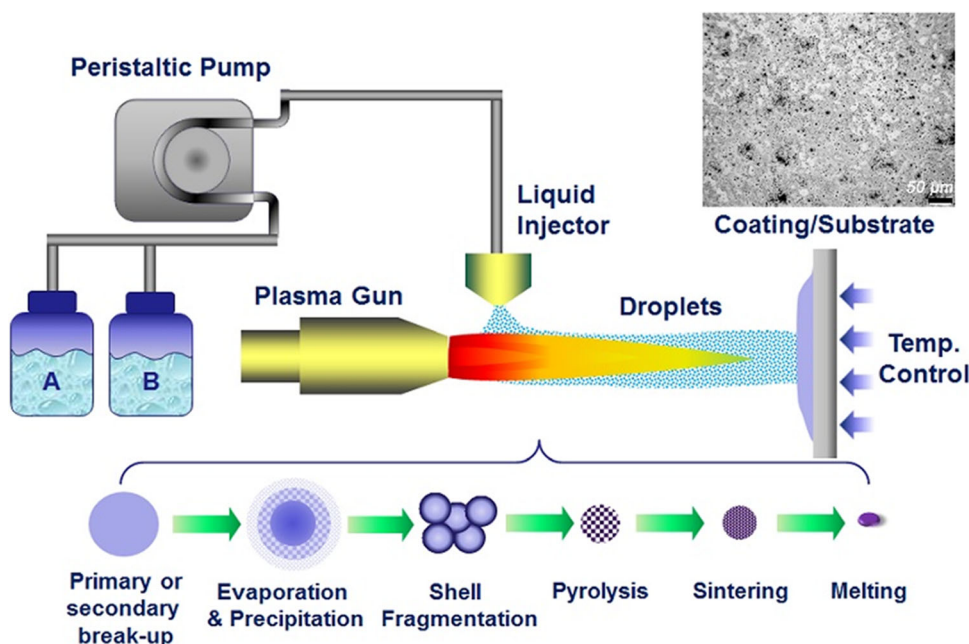
Table 1 Properties of SPPS YAG and APS YSZ coatings

TBC property	APS YSZ	SPPS YAG
Thermal conductivity (W/mK)	1.1-1.4 at 1300 °C (Ref 23)	0.58 at 1300 °C (Ref 26, 27)
Sintering resistance (50 h)	18, 43 and 59% increase in TC at 1150 , 1250 , and 1350 °C respectively (Ref 23)	4, 8 and 16% increase in TC at 1150, 1250, and 1350 respectively (Ref 23)
Thermal cycling durability	1121 °C with 1-h cycle—919 h,	1121 °C with 1-h cycles—1180 h,
	1150 °C with 8-h cycles—1152 h (Ref 23)	1150 °C with 8-h cycles—1408 h (Ref 23)
Erosion resistance	1 mm/kg at 90° and 0.91 mm/kg at 30° impingement (Ref 23)	0.57 mm/kg at 90° and 0.45 mm/kg at 30° impingement (Ref 23)
CMAS durability	Higher reactivity with CMAS (Ref 24)	Lower reactivity with CMAS (Ref 24), 15X higher with IPBs (Ref 27)
Maximum operating temperature (°C)	1200 (Ref 23)	> 1500 (Ref 23)

The purpose of part I of this work was to produce a wide range of microstructures that could be tailored to the different property requirements of the three components to be coated in part II. These processing data were transferred to Solar Turbines Incorporated (Solar) for coatings of components for rig and engine test.

Experimental Methods

Precursor Preparation

Precursor preparation of YAG (Y3Al5O12) was carried out by mixing stoichiometric amounts of yttrium (III) nitrate hexahydrate (Y(NO3)3·6H2O), aluminum nitrate nonahydrate (Al(NO3)3·9H2O) and urea in distilled water while keeping the solid loading of equivalent oxides at 130 g/L (standard, 0.22 M) or 220 g/L (concentrated, 0.37 M) of precursor. The source for all the chemicals was Alfa Aesar (Ward Hill, MA). The precursor was filtered before spraying using an inline filter (ZenPure, 10um mesh size) to remove any large solid particles and prevent clogging of stream injector.

Deposition Process for SPPS YAG TBCs

SPPS YAG TBCs were deposited using the SPPS process (shown in Fig. 1) with a Metco Sinplex Pro plasma gun with a 9 mm nozzle. No auxiliary cooling was applied to the parts during the coating process. Argon and hydrogen were used as the primary and secondary gases respectively. The precursor was delivered to the plasma gun nozzle using a peristaltic pump and fed to the plasma plume radially via either a stream injector (O'Keefe Controls Co, Trumbull, CT) which delivers a solid stream to the plasma jet where it is atomized by the cross flowing plasma or a non-atomizing fan nozzle (Spraying Systems Co., Glendale Heights, IL) that created a flat spray pattern. Different injector sizes were explored, and the choice of stream or fan nozzle will be explained in the results section. Injector tips, tipshoes and combustor liners were coated at Solar after the technology was transferred from SST. The details of spray parameter, microstructure and the rig testing are provided in the part II of the paper. A raster scan pattern was employed to coat injector tips and rub rig abradable samples while the combustor liner was coated on a rotary table while the robot moved in Z-axis, bottom to top and top to bottom. Air seal components had a curvature and to achieve a constant standoff distance with the plasma gun, the robot arm was adjusted to match the radius of curvature of the tip shoe and then swept in a very accurate circular arc controlled by the large, fixed bearing at the base of the

6-axis robot. Special fixture as shown in Fig. 28 is made to accommodate 1st and 2nd stage air seals.

For development of coatings, spray trials were conducted on SS 304 substrates (25.4 mm diameter, $\sim$ 3 mm thick) that were grit blasted with 80 mesh alumina grit at 60-70 psi resulting in a surface roughness (Ra) of 4-5 μm but not bond coated. It should be noted that the target microstructure thickness for the developmental spray was approximately 200 microns as such a thickness was sufficient to analyze the microstructure and calculate deposition efficiency and rate. To achieve this coating passes were varied from one condition to another. At the same time, it also prevented incurring additional materials costs of very thick coatings. For furnace testing, 5 mm thick Nickel Alloy H230 base metal coated with a NiCrAlY bond coat ($\sim$ 200 μm) and a thin layer of YSZ (25- 50 μm) were used for all SPPS YAG coating, and this improved durability. All the engine components were made of Nickel Alloy substrates, coated with a $\sim$ 200 μm thick NiCrAlY bond coat, and thin layer of 25-50 μm APS YSZ inner layer. Before the deposition, the substrates were preheated with the plasma gun to $\sim$ 200 °C and the temperature was measured using a probe or a welded thermocouple contacting the back side of the substrates. An optical pyrometer was used to monitor surface temperature of the combustor liner. The relevant spray parameters are shown in Table 2 largely based on the Oerlikon Metco manual.

Characterization of Coating Microstructure

Sample were sectioned using a precision Saw (Mark V Laboratory, East Granby, CT) mounted in epoxy resin (Allied High-tech Products Inc., Rancho Dominguez CA), placed under a vacuum to remove air bubbles, and left to cure at room temperature (RT). The mounted samples were ground, polished and sputter coated with Pd/Au (Polaron E5100 SEM Coating Unit) for metallography. Field emission scanning electron microscope (JSM-6350/5F, JEOL USA, Peabody MA) was utilized to analyze coatings cross-sectional microstructures and element distribution, using both the backscattered (BSE) and secondary electron (SE) modes. For determining the porosity of the coatings, image analysis was conducted using ImageJ software and compared with the porosity obtained via the weight/volume of coatings. Weight of the samples were measured before and after the spray to calculate the deposition efficiency (DE) and deposition rate (DR) of the coating process.

Measurement of Thermal Diffusivity and Thermal Conductivity (TC)

All the measurements were performed on free standing coatings, which were obtained by immersing the YAG

Table 2 Spraying parameters for SPPS YAG coatings

Spray parameters	Combustor liner	Abradability test samples	Air seals
Plasma gun	Metco Sinplex Pro		
Gun nozzle diameter (mm)	9		
Gun power (kW)	50-60		
Primary /secondary gas	Ar/H$_2$		
Gas flow rate (L/min)	Ar: 70-90, H$_2$: 5-10		
Precursor injection mode	Fan, 625 μm		
Precursor feed rate (ml/min)	70-100		
Standoff distance (mm)	50-70		
Gun scan speed (mm/s)	500-750		
Raster step size (mm)	…	2	2

coatings on SS 304 substrates in concentrated nitric acid for 12 h. Free standing coatings were rinsed with DI water to remove any absorbed acid and were dried at 80 °C for 1 h.

Specific heat measurement of YAG was measured previously (Ref 23). Thermal diffusivity measurement was performed in a range of 25-1300°C on 10 × 10 mm, 1 mm thick YAG specimens at NETZSCH Instruments North America, LLC (Burlington, MA, USA). Low temperature (25-300°C) thermal diffusivity was measured at University of Connecticut using Netzsch LFA 447 equipment. Thermal conductivity was calculated by multiplying thermal diffusivity, specific heat, and coating density. Density measurement has been described in 2.3.

Thermal Cycling

Thermal cycling was performed on SPPS YAG coatings deposited on bond-coated superalloy substrates. APS YSZ TBC baselines supplied by Solar were simultaneously tested in the furnace with the SPPS YAG samples using identical bond-coated superalloy substrates. At least three specimens of each TBCs microstructure were simultaneously cycled. Thermal cycling was conducted in a bottom-loading isothermal furnace (CM Furnaces Inc., Bloomfield, NJ) to 1150 °C using 12-h cycles with 0.5 h of ramp-up, 8 h of dwell time and 1.5 h of expedited cooling achieved by an external fan, until failure occurred. Failure was defined by ≥ 50% of coating delamination from the substrate.

Erosion Resistance

Room temperature (RT) erosion tests was conducted on APS YSZ and SPPS YAG coatings at Applied Research Laboratory, Penn State University (University Park, PA). The test conditions are listed in Table 3.

Table 3 Parameters for the erosion test conducted for the APS YSZ and SPPS YAG TBCs

Conditions	
Impact angle	90°
Particle size	50 μm alumina media (240 grit BFA)
Impact speed (m/s)	80
Standoff distance	229 mm
Mask size	12.7 mm
Feed rate	2 g/min

Determining Deposition Efficiency (DE) and Deposition Rate (DR)

Deposition efficiency was determined from the known feed rate in terms of g/hr and the geometric pattern efficiency, the spray time and the weight change of the samples from before and after spraying. Deposition rate was from sample weight before and after spray and the spray pattern efficiency and spray time.

The equations for DE and DR are as follows:

$$DE = \frac{W_c}{t * f * s * \frac{A_s}{A_g}} \tag{Eq 1}$$

$$DR = DE * f * s \tag{Eq 2}$$

where, W_c = Weight of coating; t = spray duration; f = feed rate; s = solid loading (grams of oxide/volume of precursor); A_s = Area of substrate; A_g = Area covered by plasma gun.

Results and Discussion

Demonstration of SPPS YAG with Desired Microstructures Using the Sinplex Gun

Favorable Microstructures Generated Using Sinplex Gun and Stream Injection After Experimentation with Feed Rate, Stream Injector Size and Precursor Concentration

Initial exploration with the Sinplex Pro plasma gun was carried out using a stream injector. Several plasma conditions were used (Argon/Hydrogen flow rate, current and voltage) before converging on a set of plasma conditions that resulted in promising microstructures that resembled the ones from the 9 MB gun. As is well known, hydrogen flow rate effects voltage and hence total power and hydrogen increases heat transfer to particles Effect of injector size and precursor feed rate was explored on microstructure, DE and DR. The results are shown in Fig. 2. The precursor concentration was 130 g/L. Using a larger injector with the same precursor feed rate resulted in lower DE which can be explained by lower precursor momentum and hence lower penetration in the plasma jet.

Similarly, increasing the precursor feed rate resulted in a higher DE and DR because it likely resulted in a deeper entrained precursor in the plasma jet. It is also shown that a denser microstructure is produced with a lowest DE value and is contrary to what is usually observed in thermal spray. The reason for such a behavior is likely a deeper entrained precursor results in an aggressive droplet breakup and smaller drops result in particles being diverted off the sample as they follow the gas stream (Stokes number effect) and more shadowing.

A higher concentration precursor (220 g/L versus 130 g/L) was also explored using a 300-micron injector. The viscosity of low and high concentration precursors were 0.0048 and 0.0142 Pa s respectively at room temperature. The resulting microstructure, DE and DR values are shown in Fig. 3 and the coating with lower feed rate (Fig. 3a) is denser than the higher feed rate (Fig. 3b). The DE values are similar to the coatings shown in Fig. 2, however, the DR values were significantly higher because of higher solid loading of the precursor. It is also noted that the thickness of coatings shown in Fig. 3a and 3b are 150 microns and 260 microns, respectively. The DE for both the figures are same, however increased DR (Fig. 3b) leads to a thicker
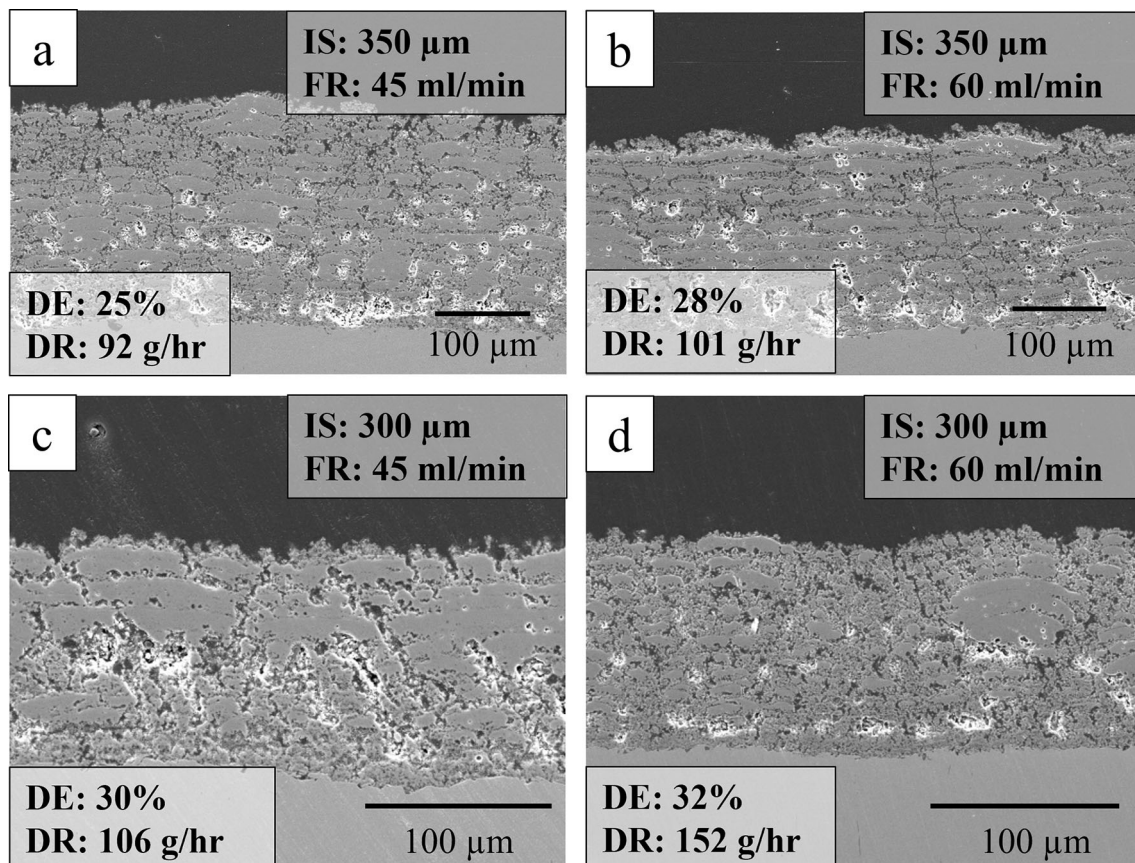

Fig. 2 Optimization of SPPS YAG coatings with varying precursor feed rate and precursor injector size, precursor concentration is fixed at 130 g/L. Injector size (IS) and precursor feed rate (FR) is provide for each of the four microstructures
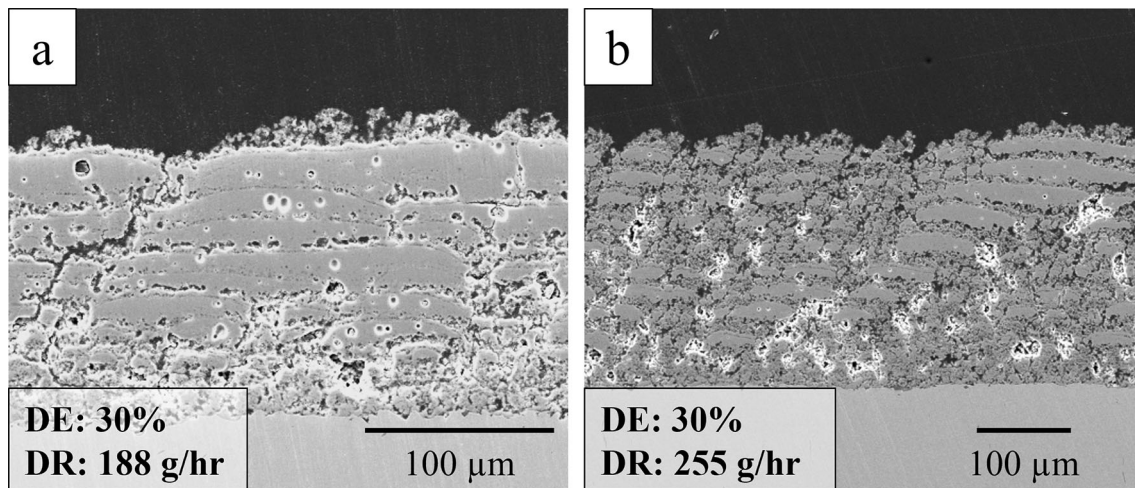
Fig. 3 SPPS YAG microstructure with higher concentration precursor (220 g/L) and a 300-micron injector. Precursor feed rate of 45 ml/min and 60 ml/min was used for (a) and (b) respectively

Table 4 Spray parameters for the initially optimized SPPS YAG microstructure with Sinplex Pro plasma gun using a stream injector

Spray parameters	Sample A (Fig. 4a)	Sample B (Fig. 4b)
Plasma gun	Metco Sinplex Pro	Metco Sinplex Pro
Gun nozzle diameter (mm)	9	9
Precursor concentration (g/L)	130	220
Precursor injector|Size (µm)	Stream|350	Stream|350
Gun power (kW)	54	53
Primary /secondary gas	Ar/H_2	Ar/H_2
Gas flow rate (L/min)	Ar: 90|$_2$: 6	Ar: 85|H_2: 6
Precursor feed rate (ml/min)	45	60
Standoff distance (mm)	56	52
Gun scan speed (mm/s)	550	550
Raster step size (mm)	2	2

coating. Results from Fig. 2 and 3 are used to down select, precursor concentration, injector size and precursor feed rate for further optimization of microstructure and property generation. Two microstructures were deemed desirable, a) dense coating and b) coating with prominent IPBs. For the dense coatings, exact spray conditions of Fig. 2(a) are employed and for the prominent IPBs, modified conditions from Fig. 3(b), with a larger injector was used. The detailed spray parameters are provided in Table 4. The two down selected microstructures are shown in Fig. 4 where (a) has higher density and (b) is more porous with a higher density of IPBs.

Property Generation with Optimized Coatings

Thermal conductivity (TC) of freestanding coatings from Fig. 4 is shown in Fig. 5. Both samples show a typical decreasing TC trend with increasing temperature, as is expected for YAG. The sample A shows TC values of 1.6 W/mK and 1.3 W/mK at RT and 300 °C respectively while sample B which has 1.2 W/mK and 1.1 W/mK at RT and 300 °C respectively. Thus, TC of microstructure B that is 38% and 25% lower than microstructure A at RT and 300 °C respectively. To explain this stark difference in TC values high magnification images are provided in Fig. 6. Microstructure A has a 22% porosity as compared to microstructure B (27% porosity), which does contribute to its higher TC however the main reason for lower TC of microstructure B is due to having twice as wide porous regions in the layered structure as compared to A (8 µm versus 4 µm). It has been shown in the past that IPBs can be up to 70% porous (Ref 26) and the concentration of porosity in layers locally results in a greater reduction of effective conduction area and for a given overall porosity density greater reduction in thermal conductivity (Ref 41).

Thermal cycling results are provided in Fig. 7 and demonstrates that both YAG samples performed superior to that of the YSZ baseline. The failure modes in all the TBCs,
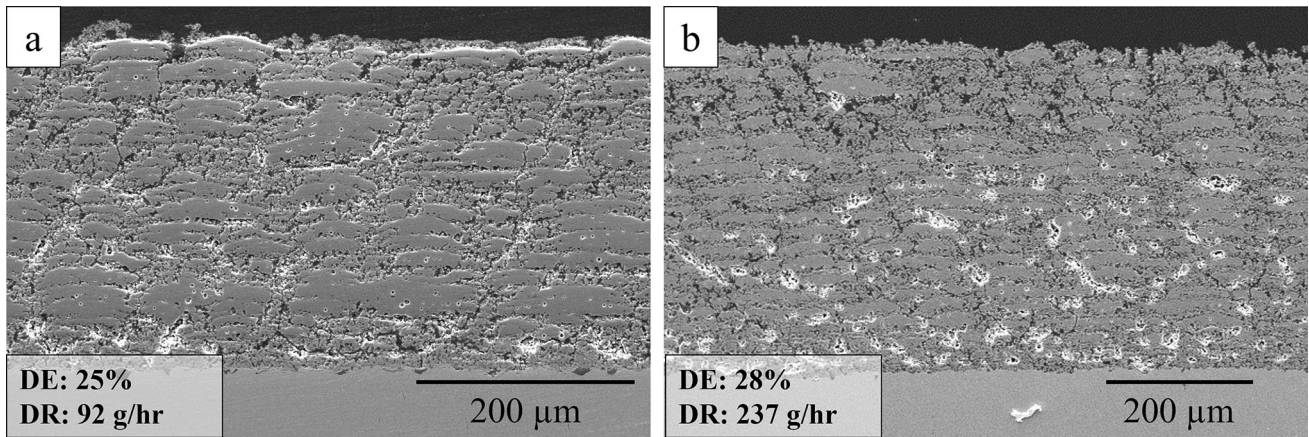
Fig. 4 Initially optimized microstructure of SPPS YAG with Sinplex Pro plasma gun using a stream injector. Detailed spray parameters are provided in Table 4

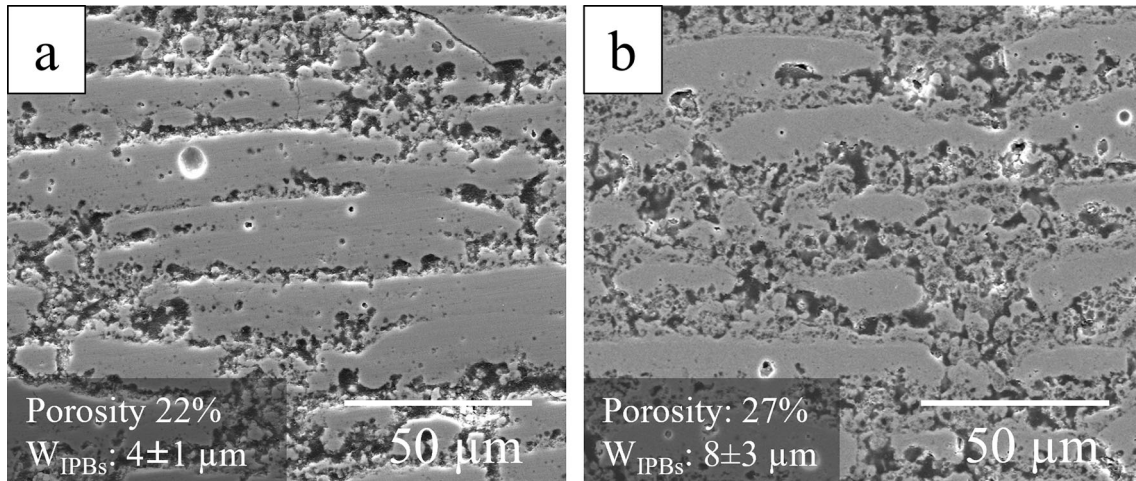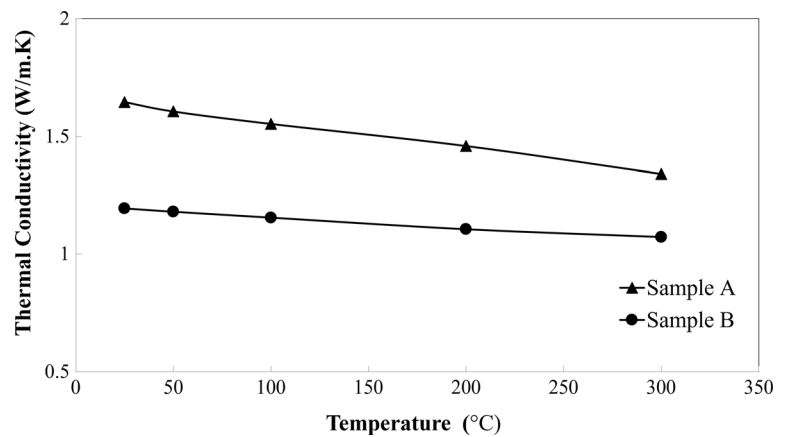**Fig. 5** Thermal conductivity of optimized microstructures shown in Fig. 4

Fig. 6 Magnified images of microstructures shown in Fig. 5

not shown here, were black in nature and the failure occurred at the thermally grown oxide (TGO)-TBC interface.

Erosion test results are presented in Fig. 8 and depict that the YAG samples can show greater erosion rates than the APS YSZ baseline. YAG microstructure A, which is denser of the two YAG coatings, performed better and had a 1.2X erosion rate as compared to the baseline, while the microstructure B performed 1.7X worse than the baseline.

The presence of IPBs and high porosity in the IPBs lead to faster erosion rates in the microstructure B. Subsequently a dense outer layer is added to enhance erosion resistance. The IPBs in Fig. 4(a) and 6(a) might appear more discernable to the readers because they are narrower (4 microns) as compared to the IPBs in Fig. 4(b) and Fig. 6(b) which are wider (8 microns) providing a stark contrast between the dense and IPBs regions. Wider IPBs offers lower thermal conductivity but worse erosion rates, thus preference for either of the microstructure would be application based. We note all SPPS samples have vertical cracks but do well in erosion when dense.

SPPS YAG with Extremely Low Thermal Conductivity and Enhanced Deposition Rate

Results from Taguchi Design of Experiments

Spray trials were conducted based on the Taguchi L8 orthogonal array with a two-level design to find conditions for coatings with extremely low thermal conductivity and enhanced deposition rate. For low thermal conductivity two factors in the coating microstructure (Ref 26, 27) are
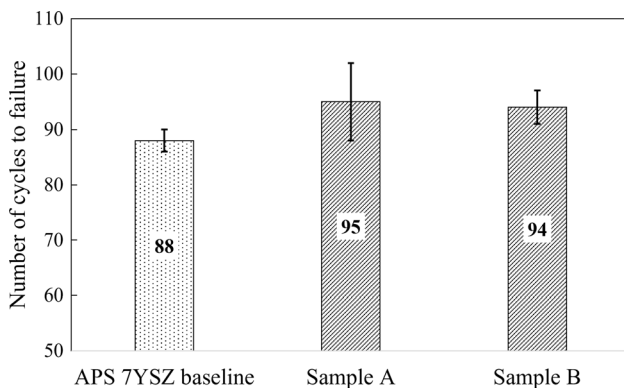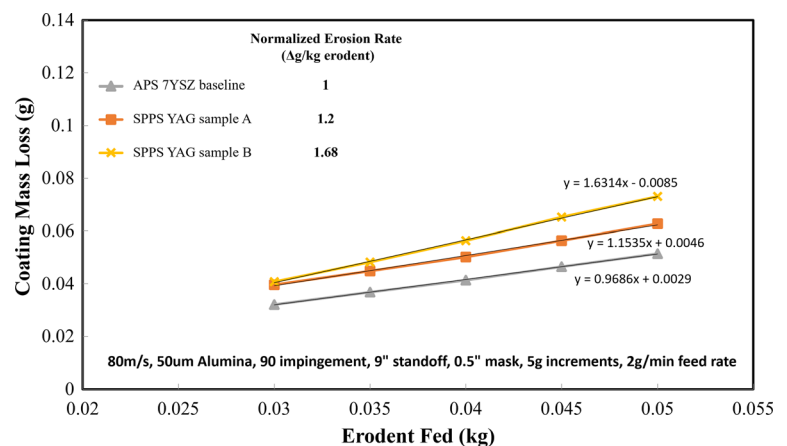
critical, prominence of IPBs and overall coating porosity. Previous studies on SPPS YAG have demonstrated that IPBs can be engineered, and their prominence can be altered by precursor feed rate, plasma power and step size in a raster scan motion of the robot. For a higher deposition rate, a higher precursor feed rate is necessary. With the aforementioned knowledge, five processing variables were chosen, namely, precursor feed rate, current, hydrogen flow rate, precursor injector size and step size and two values for each of the variables were chosen. Argon flow rate (90 L/min) and robot scan speed (500 mm/s) were fixed for all the spray trials. The responses for the Taguchi design were DE, DR, coating porosity and IPB prominence. A value of 0, 5 or 10 was assigned for the IPB prominence by observing the coating microstructure. A coating with no appearance of IPBs was given a value of zero and the ones that showed very prominent IPBs were given a value of ten. Microstructures that did show IPBs but were not very prominent were given a value of five. The idea of such an exercise was to identify the key variables that affect the IPBs formation. The values of the variables are provided in Table 5 along with the responses. The microstructures generated during the Taguchi trials are shown in Fig. 9 where images (a) to (h) correspond to spray trial 1 to spray trial 8 respectively.

As shown in Table 5 and Fig. 10, the deposition rates vary from 228 to 422 g/hr. which is at least 2X higher than the initially optimized microstructure shown in Fig. 5. This is a direct consequence of employing higher precursor feed rates. The porosity of the microstructures ranges from 30-50% which is on the higher end for a TBC. Despite showing higher porosity levels, only microstructures shown in Fig. 10(b) and (d) show prominent IPBs. However, Fig. 10(b) features the lowest DE and DR. Based on these results the coating from spray trial 4 (Fig. 10d) was selected for further optimization.

To understand the effect of Taguchi variables on the responses, namely porosity, IPB prominence and

Fig. 7 Thermal cycling performance of optimized SPPS YAG coatings as compared to APS 7YSZ baseline

Fig. 8 Erosion performance of optimized SPPS YAG coatings as compared to APS 7YSZ baseline

Table 5 Taguchi L8 orthogonal array design for porous SPPS YAG coatings with values of process variables and the responses

Taguchi L8 Orthogonal Array Design								
Spray trial #	ST1	ST2	ST3	ST4	ST5	ST6	ST7	ST8
Variables								
Feed rate (mL/min)	75	75	75	75	100	100	100	100
Current (A)	500	500	535	535	500	500	535	535
H2 flow rate (lpm)	7	7	8	8	8	8	7	7
Injector size (microns)	350	400	350	400	350	400	350	400
Step size (mm)	1	2	1	2	2	1	2	1
Responses								
Average DE (%)	34	23	32	26	29	26	32	31
Average DR (g/hr.)	337	228	317	257	383	343	422	409
Porosity (%)	35	34	39	30	50	34	43	43
IPB prominence	0	10	5	10	0	5	0	0
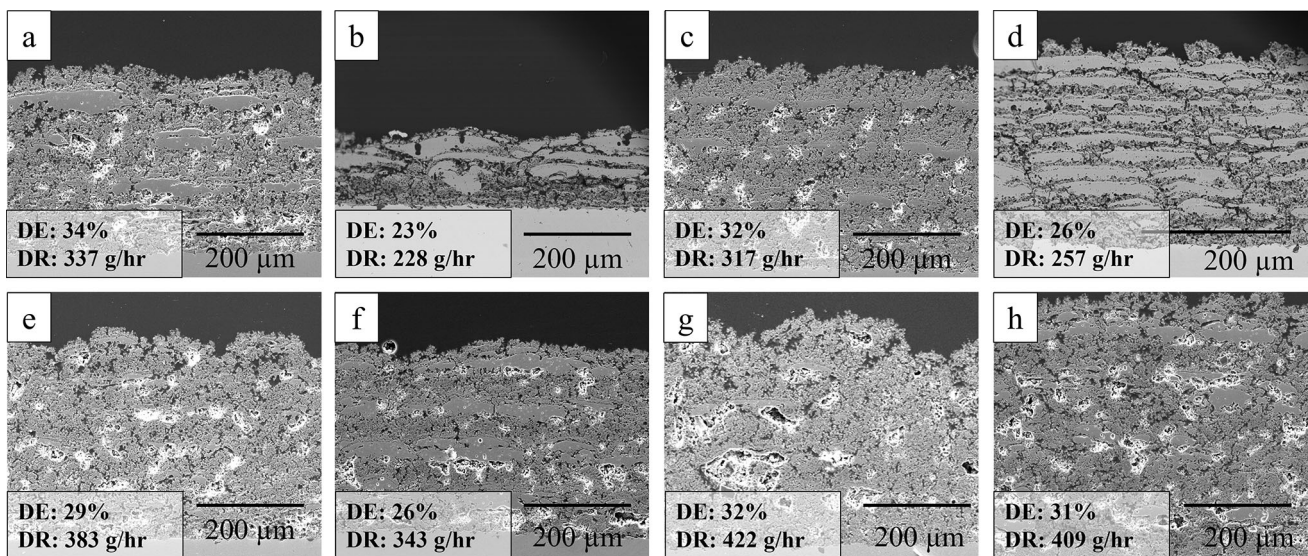
Fig. 9 Microstructures generated during a Taguchi L8 orthogonal array trial for obtaining SPPS YAG TBCs with ultra-low thermal conductivity with high DR

deposition rate, Main Effect plots are a valuable tool which demonstrate the effect of each of the variables on the responses. These can then be ranked as to importance. Such plots are provided in Fig. 11. Each variable is plotted between 1 and 2, which correspond to lower and higher values of the variable respectively. A positive slope demonstrates increasing trend of a response with increasing value of the variable and vice versa. Coatings porosity is highly affected by precursor feed rate and injector size. Higher feed rate results in a more porous coating and a larger injector reduces porosity. A possible explanation for this is that a more entrained precursor would go through more aggressive droplet breakup resulting in smaller droplets, more shadowing and hence results in a more porous microstructure and lower DE. Increasing raster step size increases coating porosity which is likely because of lower

heat transferred to the substrates and the coatings between subsequent raster scan steps.

IPBs prominence seem to be affected most and equally by precursor feed rate and injector size. Feed rate inversely affects IPBs prominence as the larger stream momentum associated with a high feed rate penetrates the plasma jet more. It has been shown that the un-entrained precursor that resides on the periphery of the plasma jet and reaches the substrate partially unpyrolyzed results in the IPB formation (Ref 27). A larger injector results in less penetration and more semi pyrolyzed materials on spray periphery and hence enhances IPBs formation. In addition, two variables that affect the IPB formation is hydrogen flow rate and step size. A larger raster step size seems to enhance IPB formation which is opposite of what was found in the previous study (Ref 27). Such is not the case in the current study and
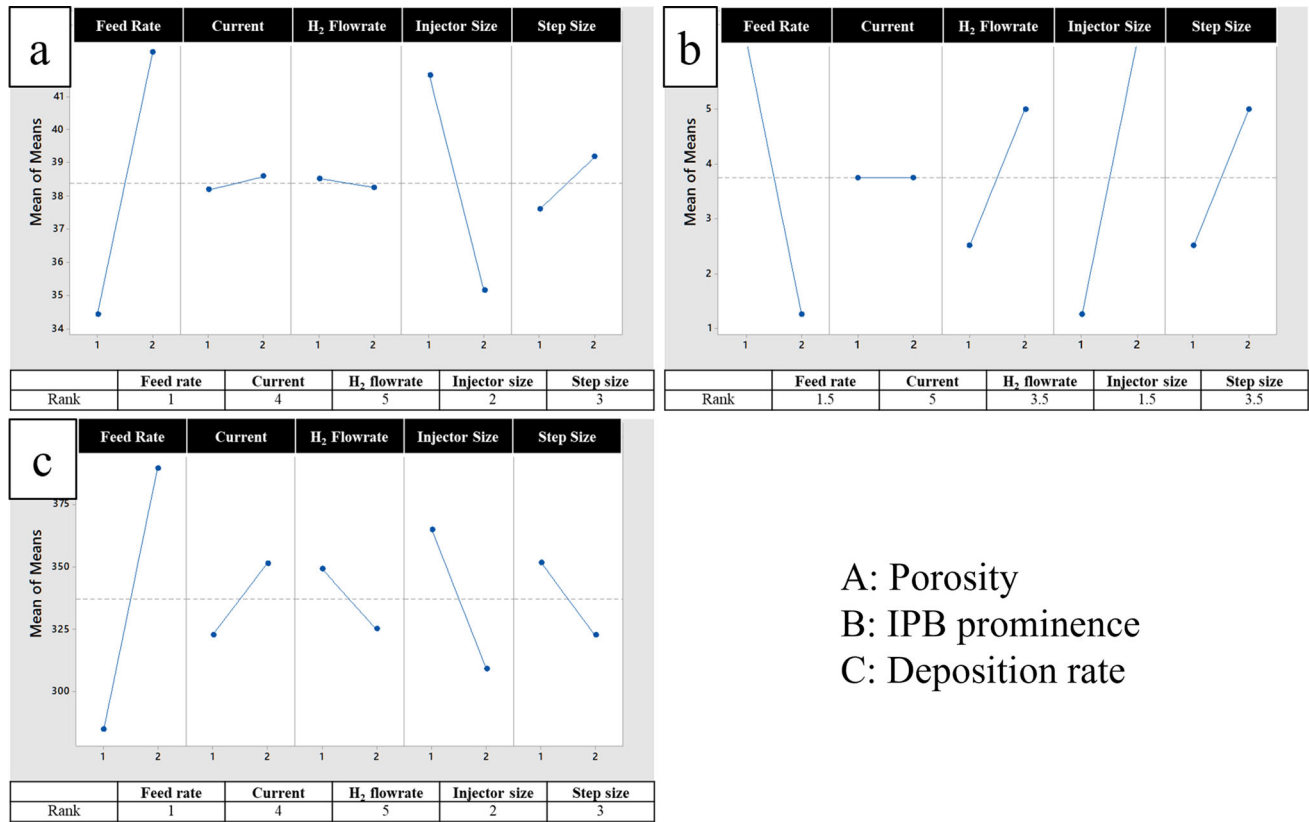
Fig. 10 Main effects plot demonstrating the effect of different plasma spray variables on (a) coating porosity, (b) IPB prominence, and (c) deposition rate
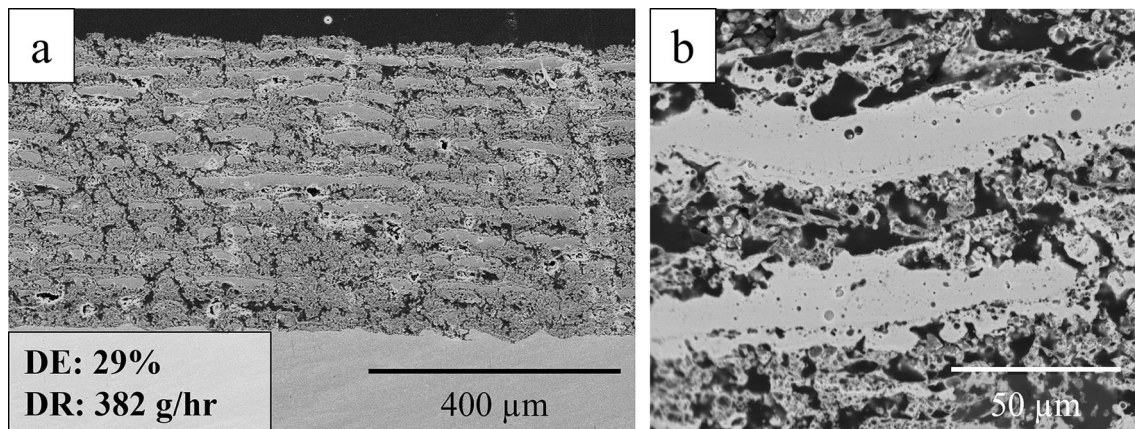

Fig. 11 Optimized SPPS YAG coating for ultra-low thermal conductivity

is likely that the spray pattern generated by the Sinplex pro gun with a stream nozzle is different from the atomized droplets used with the 9 MB gun in the previous study (Ref 23). Hydrogen flow rate was chosen as one of the parameters as it affects the voltage and power of the plasma jet. As per Fig. 10, hydrogen has a lower impact (Rank 3.5) on IPB formation as compared to precursor feed rate and injector size. With increasing H2 flow rate, the prominence of IPBs seem to increase. It is suggestive that an increase in

H2 flow rate increases the conductivity of the plasma jet and in turn increases the heat transfer from the plasma to the substrate. This may lead to pyrolyzation of the semi-pyrolyzed precursor that reaches the substrate, which has been shown to be responsible for IPB formation in our previous study (Ref 27).

The principal factor affecting DR is precursor feed rate as more precursor is used per unit time to deposit the coatings. This is followed by the injector size where a

bigger injector size reduces DR, which is explained by lower penetration of precursor in the plasma jet and poorer heating of the precursor. H2 flow rate affects the DR the least. We are unsure of the underlying mechanism.

Optimized Microstructures and Thermal Conductivity Measurement

Based on the coatings produced during the Taguchi trials, as shown in Fig. 9, microstructure from spray trial 4 (Fig. 9d) was selected for further development due to the strong IPB presence in the microstructure, leading to the expectation of lower thermal conductivity. All the spray parameters were kept the same, except the feed rate which was increased to 100 ml/min. It is noted that the prominence of IPBs reduce with increasing precursor feed rate as shown in Fig. 10(b), however, increasing feed rate was a deliberate choice to increase DR and overall porosity. A more porous coating would result in a lower thermal conductivity. The resultant microstructure is shown in Fig. 11. Since a higher feed rate was employed, both the DE and DR values went up from 26 to 29% and from 257 g/hr to 382 g/hr. The overall coating porosity also increased from 30 to 45%. Width of IPBs as shown in Fig. 11(b), 24 ± 6 μm which is 3X wider than the for the coating shown in Fig. 6(b). The thermal conductivity measurement of a freestanding coating is shown in Fig. 12, with the same microstructure of Fig. 11, resulted in a room temperature value of 0.54 W/mK and 0.48 W/mK at 1300 °C, which is the lowest recorded for SPPS YAG. As compared to the specimens shown in Fig. 4 and 6, a drastic reduction in thermal conductivity was achieved because of the following two factors:

A. Increasing the overall porosity of the coatings (45% for Fig. 11 versus 22% and 27% for Fig. 4(a), 6(a) and Fig. 4(b), 6(b), respectively)

B. Significantly increasing the width of the IPBs (24 ± 6 μm for Fig. 11 versus 4 ± 1 μm and 8 ± 3 μm for Fig. 4(a), 6(a) and Fig. 4(b), 6(b), respectively.)

Highly Dense and Hard Coatings for Enhanced Erosion Resistance

The development of dense coatings was initiated using the opposite approach to that used in generating porous coatings. The approach for denser TBCs employed lower feed rates (25-45 ml/min) and a larger orifice (350 and 400 μm) for precursor injector. A total of twelve spray trials were conducted and all the trials resulted in either porous or discontinuous microstructures accompanied by extremely low DR. To produce dense coatings, a precursor injector which produced a fan-shaped precursor pattern was employed. The BETE nozzle produced a cone spray pattern while this pressure nozzle produced a flat fan pattern. A schematic of the fan nozzle is shown in Fig. 13 where left side shows the spray setup of a fan nozzle with respect to the plasma torch and right side shows the fan nozzle and the ejecting precursor in the shape of a "fan".

The idea of fan nozzle was conceived to utilize the entire plume width of the plasma jet. A stream nozzle injects the precursor in the dead center of the plasma jet where the precursor gets broken up into smaller droplets that experience pyrolysis. However, the peripheral regions of the plasma jet and its energy are mostly wasted. With a fan nozzle (Fig. 13, right), ejected precursor diverges from the point of exit and at the ideal radial distance from the plasma jet the width of the fanning precursor is of comparable width to the diameter of the plasma jet.

Initial experiments were conducted with 425 μm sized fan nozzle, capable of a maximum delivery of 55 ml/min. To find the ideal radial distance for the future spray trials, three spray trials were conducted with the same spray
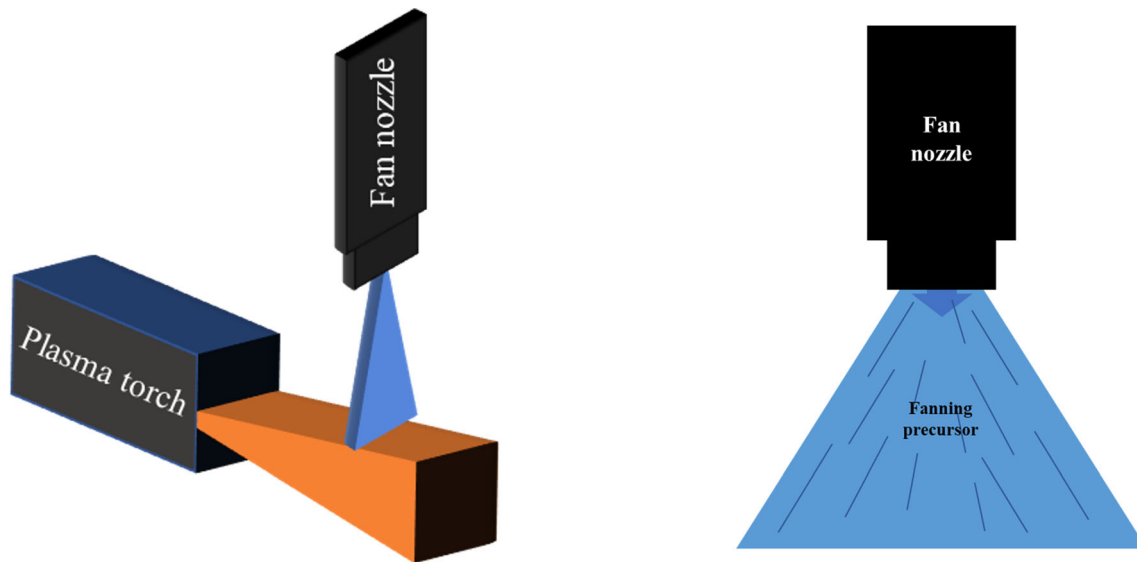
Fig. 12 Thermal conductivity of optimized microstructure
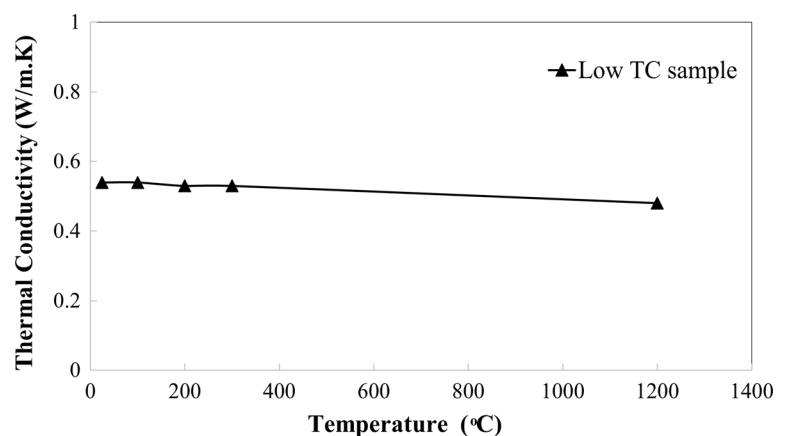
Fig. 13 Schematic of a fan nozzle setup on the left and fan nozzle on the right with precursor ejecting in a fan pattern
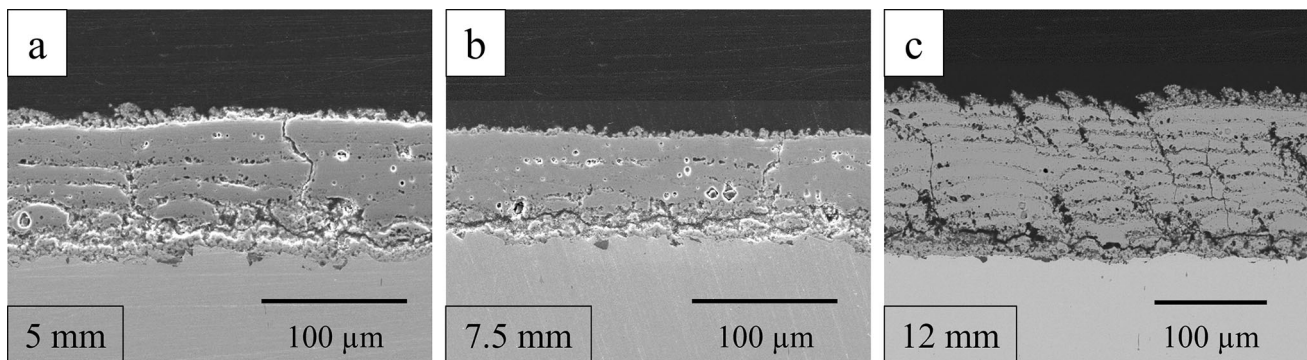

Fig. 14 Microstructures of SPPS YAG coatings using a fan nozzle (smaller, 425 µm) with varying radial distance from the gun nozzle

parameters, where radial distances from the gun nozzle were 5, 7.5 and 12 mm. The generated microstructures are shown in Fig. 14. The DE for the three trials were 33, 34 and 36% indicating increased utilization and deposition of precursor on the substrates with increasing radial distance, however with increased DE, the overall porosity in the case of SPPS process increases. The densest coatings were obtained using a radial distance of 7.5 mm and 7.5 mm was chosen for all further trials. It is note that despite of the highest DE obtained with 12 mm radial distance, the overall coating porosity increased as compared to 5 and 7.5 mm radial distance. In the case of SPPS process, there is not a strong correlation between the DE and coating density.

The next set of trials were conducted using a larger (625 µm) fan nozzle and feed rates of 75 and 100 ml/min were used. The microstructures obtained were dense (Fig. 15), similar to that of the smaller fan nozzle with DE values of 34% and 29% respectively. However, a larger fan

nozzle offered a higher manufacturer recommended precursor flow rate and thus a higher DR as compared with the smaller fan nozzle while producing similar dense microstructures hence was used for further optimization of dense coatings. The spray parameters for initial set of experiments using the larger fan nozzle (625 µm) are provided in Table 6.

To further increase the density of the coatings and understand the effect of certain parameters on the microstructure using a fan nozzle a L8 orthogonal array Taguchi trial (Table 7) was designed based on the previous experiments where three variables were chosen, namely precursor feed rate, total plasma gas flow rate (argon + hydrogen), and raster scan step size. The ratio of Ar/H2 was fixed to 10, current was set to 525 amperes (same value was used for smaller fan nozzle and Table 6), radial distance was 7.5 mm, and the larger fan nozzle was used. The microstructures obtained from the Taguchi trials are shown in Fig. 16 where (a) corresponds to spray 1 and
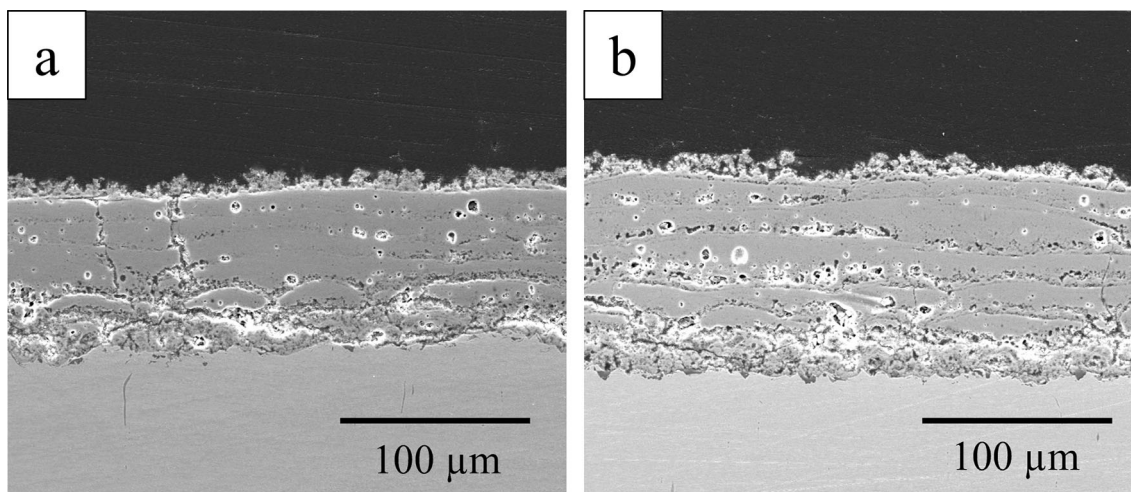
Fig. 15 Microstructure of SPPS YAG coatings using a larger (625 μm) fan nozzle with (a) 75 ml/min and (b) 100 ml/min precursor feed rate

Table 6 Spray parameters for initial set of experiments using larger (625 μm) fan nozzle

Spray parameters	
Plasma gun	Metco Sinplex Pro
Gun nozzle diameter (mm)	9
Gun power (kW)	55
Primary/secondary gas	Ar/H$_2$
Gas flow rate (L/min)	Ar: 85, 71‖H$_2$: 7, 7 (Trial 1 and Trial 2 respectively)
Precursor injection mode	Fan, 625 μm
Precursor feed rate (ml/min)	75,100 (Trial 1 and Trial 2 respectively)
Standoff distance (mm)	51
Gun scan speed (mm/s)	550
Raster step size (mm)	2

Table 7 Taguchi L8 orthogonal array design for dense SPPS YAG coatings with values of process variables and the responses

Taguchi L8 Orthogonal Array Design								
Spray trial #	ST1	ST2	ST3	ST4	ST5	ST6	ST7	ST8
Variables								
Feed rate (mL/min)	80	80	80	80	110	110	110	110
Ar + H2 flow rate (lpm)	78	78	93	93	78	78	93	93
Step size (mm)	1	2	1	2	2	1	2	1
Responses								
Porosity (%)	15	12	17	10	18	14	19	12

so on. Using the spray parameters shown in Table 7, the densest microstructures were obtained with porosity ranging between 10 and 19%. Interestingly, a step size of 1 mm produced more prominent IPBs as compared to a step size of 2 mm which produced uniformly dense coatings opposite to what was the case with the stream injector. The Main Effects plot for coating porosity (shown in Fig. 17) demonstrates that feed rate was the prominent factor determining the coating porosity. It is noted that the microstructures obtained in Fig. 15 through Table 6

conditions appeared homogenously denser than the ones obtained in Fig. 16 using Table 7 conditions. Thus, microstructures shown in Fig. 15 are deposited on a superalloy sample with thin APS YSZ inner layer. The superalloy substrates were significantly rougher (10-11 Ra) than the grit blasted SS 304 substrates (5-7 Ra) thus making the microstructure not exactly replicable. The erosion samples are shown in Fig. 18 and their erosion performance are presented in Fig. 19. As compared to the baseline samples one YAG sample performed superior
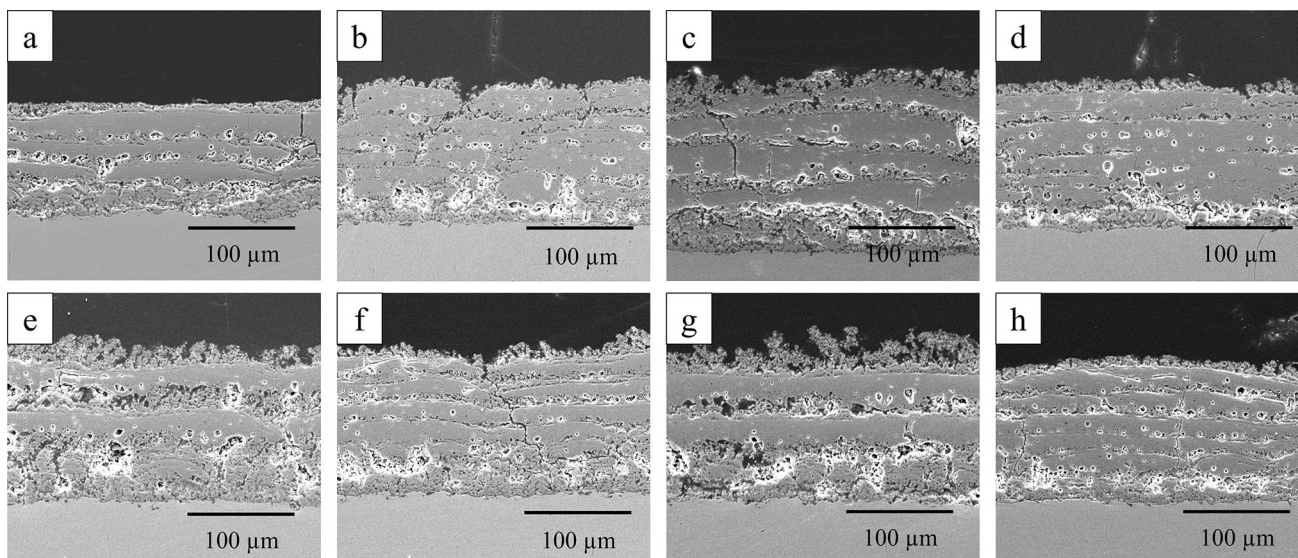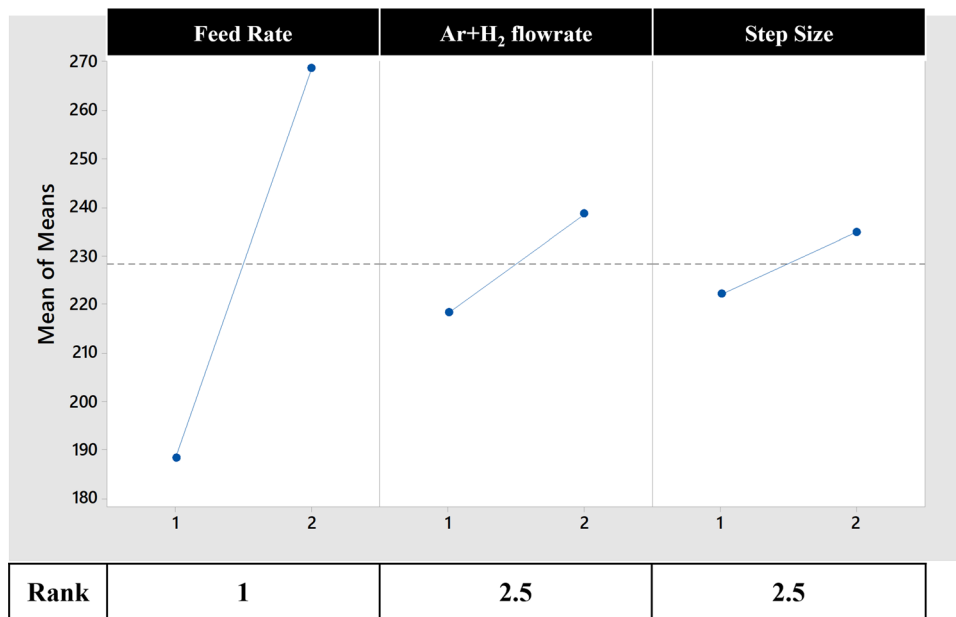
Fig. 16 Microstructures generated during a Taguchi L8 orthogonal array trial for obtaining SPPS YAG TBCs with low porosity using a larger (625 μm) fan nozzle

Fig. 17 Main effects plot demonstrating the effect of different plasma spray variables on coating porosity using a larger (625 μm) fan nozzle

(0.7X, normalized WRT. baseline) and another sample performed slightly worse (1.1X) in the erosion test. Room temperature thermal conductivity values of microstructures shown in Fig. 18(a) and (b) are 1.7 and 1.6 W/mK respectively, which is expected for a dense coating without prominent IPBs. Thus, using the fan nozzle, dense, erosion resistant SPPS YAG coatings were successfully developed. There is a clear tradeoff between minimum thermal conductivity and erosion resistance. This leads to using different microstructures for different components, and to the use of a dense top layer for better erosion resistance.

Demonstration of a Coating with Varied Porosity

Using the techniques for depositing porous and dense YAG coatings, as demonstrated in previous two sections, a coating with graded porosity was explored. Larger fan nozzle was used for this study. Two variations of such microstructures were developed, one where the porosity of the coating was continuously increased from substrate to the surface and second where a thick porous middle layer was sandwiched between a thin dense bottom and top layers. In a published study (Ref 42) dense inner layer was shown to produce increased cyclic life. Similarly, in a
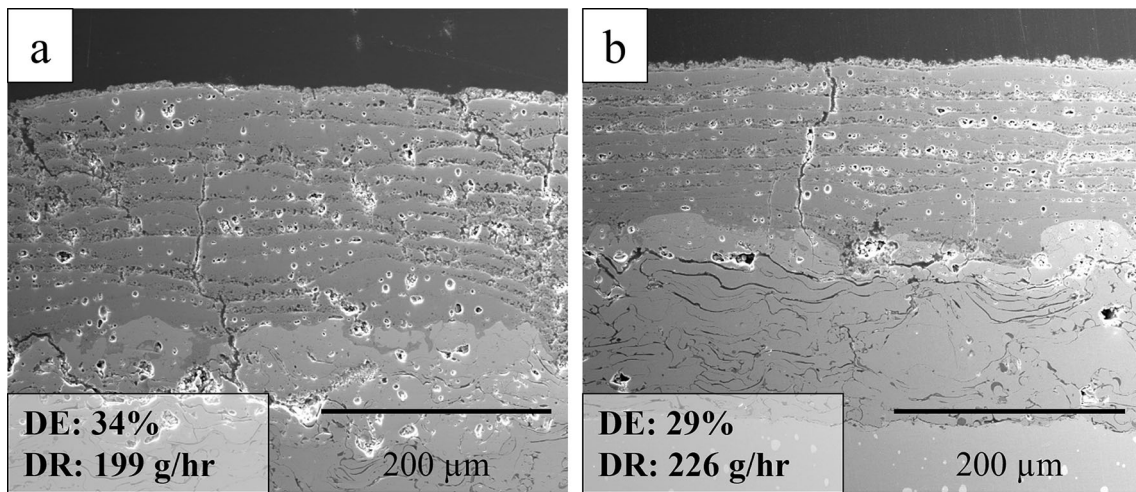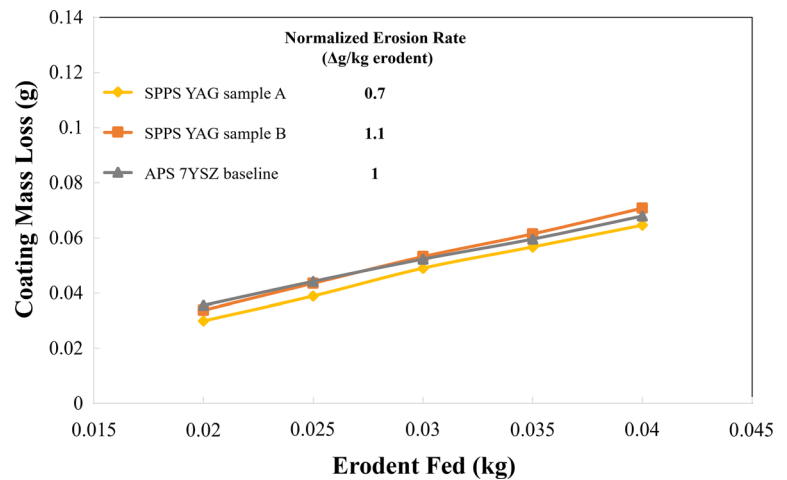
Fig. 18 Optimized SPPS YAG dense coatings for improved erosion resistance using a larger (625 μm) fan nozzle

Fig. 19 Erosion performance of optimized dense SPPS YAG coatings using a larger (625 μm) fan nozzle as compared to APS 7YSZ baseline

continuously graded coating, the dense bottom layer was expected to enhance durability during thermal cycling and a porous top layer would be used for abradability properties, as required for the air seals in the upcoming sections. The development of a 3-layered coating was for the coating of inner combustor liners, where the dense bottom layer would provide durability during thermal cycling, the thick middle porous layer would ensure lower thermal conductivity and a thin dense top layer would provide erosion protection.

These microstructures are shown in Fig. 20. For a continuously graded coating, five different combinations of precursor feed rate (75-100 ml/min) and standoff distance variation (50-70 mm) was used as shown in Table 8. Longer stand off distance and higher feed rate resulted in a more porous coating. All other parameters were kept constant. Similarly, the dense layers in the 3-layered coating were produced with lower feed rate and shorter standoff distance while the opposite was employed to

produce the thick porous layer. The porosity of the dense layers was between 15 and 20% while for the porous layer was 30-35%.

The results of the thermal cycling performed on these coatings are presented in Fig. 21 and both YAG samples outperformed the APS YSZ baseline. The failure modes (not shown here) were black in nature and due to the TGO growth with separation between the ceramic and TGO interface. In the case of the 3-layered coating, secondary failure between the dense bottom and the middle porous layers was also observed. Later the efficacy of the bottom dense layer was explored both at SST and Solar and it was found that the dense layer on the graded coating provided only a marginal benefit in thermal cycle life. The average cycling life with and without the thin dense layer were 86 and 83 at SST and 94-106 cycles and 94 cycles at Solar respectively. For replicating the coating on a combustion liner, the initial dense region was not applied to reduce process complexity without debiting coating durability.
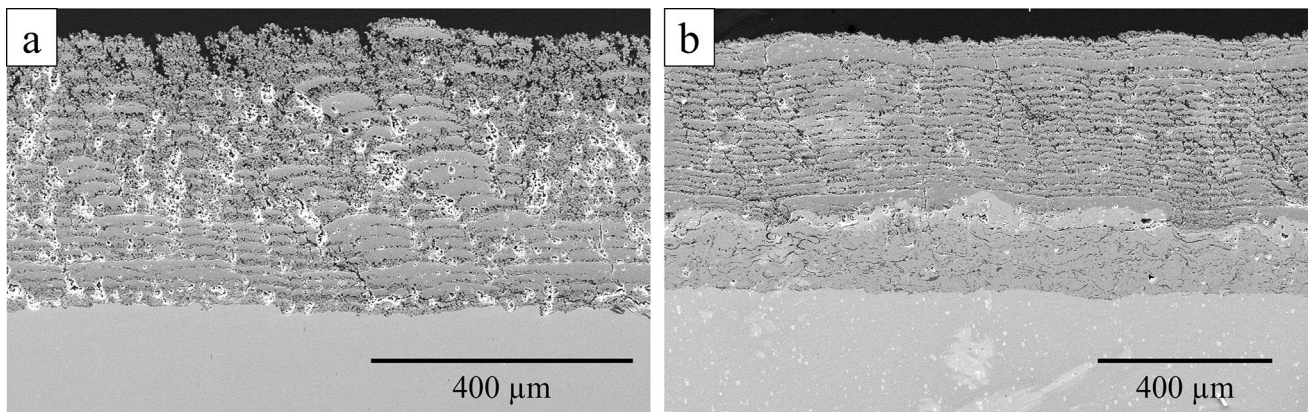
Fig. 20 SPPS YAG coatings with (a) continuously graded porosity and (b) layered porosity

Table 8 Detailed spray parameters for producing graded and layered coatings shown in Fig. 20

| Spray parameters	Continuously graded	Layered
Plasma gun	Metco Sinplex Pro	Metco Sinplex Pro
Gun nozzle diameter (mm)	9	9
Precursor concentration (g/L)	130	130
Precursor injector | Size (μm)	Fan|625	Fan|625
Gun power (kW)	55	53
Primary /secondary gas	Ar/H$_2$	Ar/H$_2$
Gas flow rate (L/min)	Ar: 71||H$_2$: 7	Ar: 85||H$_2$: 6
Precursor feed rate (ml/min)	75 (Bottom), 75, 100, 100, 100 (Top)	75 (Bottom & Top) 100 (Middle)
Standoff distance (mm)	50, 50, 50, 57, 64	50 (Bottom & Top) 57 (Middle)
Gun scan speed (mm/s)	550	550
Raster step size (mm)	2	2
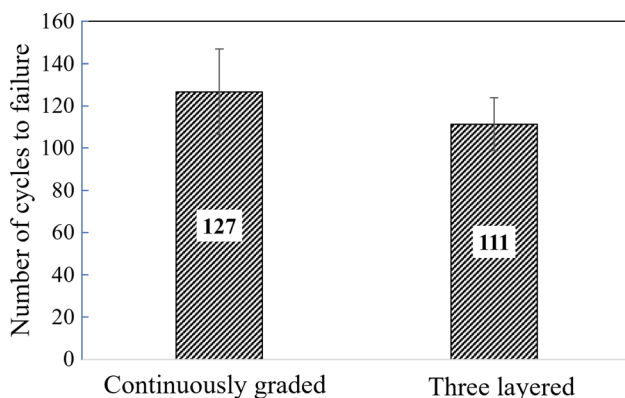
Fig. 21 Thermal cycling performance of (a) continuously graded porosity YAG and (b) layered porosity YAG

Development of Coatings for Annular Combustor Liner

In developing a SPPS YAG coating process for an annular combustor liner, a scrap liner was used with attached coupons. This was needed because of the very different thermal response of this large part and the use of a rotating table in place of robot-based raster scanning. This minimized the effort at Solar to utilize the processes developed at SST. At the same time process microstructure trends from prior experiments were critical to guide this development. The liner was made of H230 nickel alloy with a diameter of 51 cm and a height of 35 cm. After each spray event, cut outs were obtained from the liner which were used for metallography. Coupons were used for assessing the thermal cycling performance of the coating The biggest challenge for coating the liner were to maintain a desirable surface temperature (250 °C) because of its large surface area. An optical pyrometer was used to monitor and control coating surface temperature and two 1.5 KW auxiliary infrared heating lamp that projected a vertical line of heat on the full height of the liner were used to maintain part temperature. Figure 22(a) shows the image of the scrap liner with coupons attached, inset shows cutout of the liner and Fig. 22(b) shows the schematic of the liner during the

Fig. 22 (a) A scrap liner with coupons attached, inset shows cutout of the liner post spray and (b) shows the schematic of the liner during the spray with an infrared heating lamp and pyrometer for surface temperature measurement
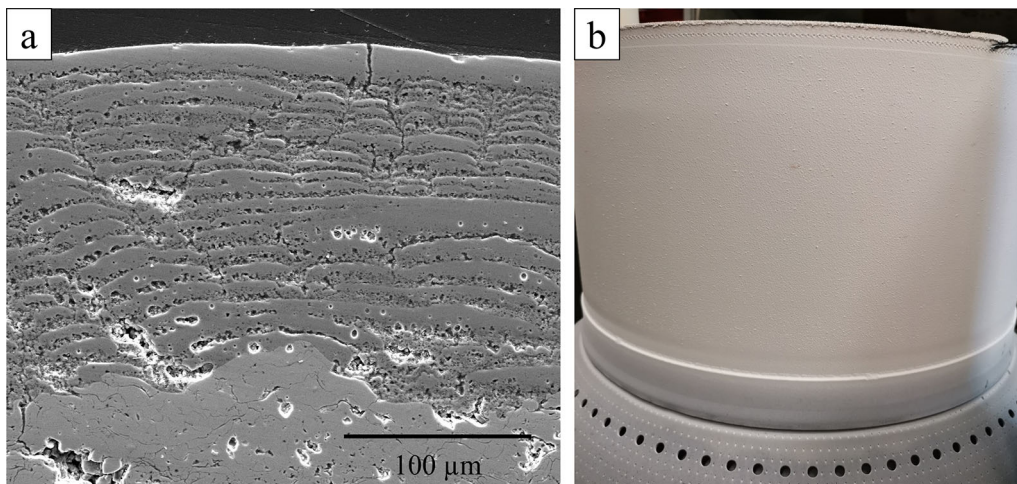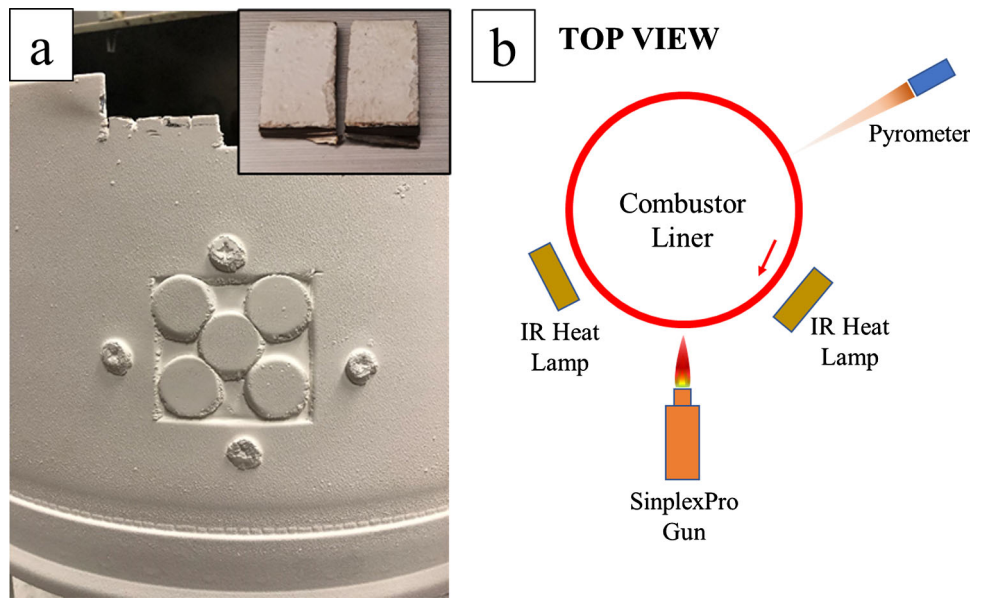

Fig. 23 SPPS YAG coating on a simulation liner, (a) coating microstructure and (b) coated liner post spray

spray with an infrared heating lamp and pyrometer for surface temperature measurement.

Once the development of the spray parameters was completed, a new scrap liner (Fig. 23b) was coated in a practice run. The targeted microstructure with thick porous (25-35%) inner layer and a thin dense layer (10-15%) was successfully achieved (Fig. 23a). After this spray, a Titan 250 annular combustor liner was similarly coated (Fig. 24c) with 500 microns of SPPS YAG and the microstructures were obtained from a coupon attached to the top of the liner. The targeted microstructure is achieved as shown in Fig. 24(a) and (b). The very dense layer on top for erosion resistance was produced by adjusting the spray parameters based on our understanding of process-properties relationship.

Deposition of Abradability Test Samples

YAG coating for turbine outer air seal applications targeted a layered coating with a dense inner layer for durability and a porous outer region for abradability. Coating abradability is required to minimize blade wear during a rub or inter-action at operating conditions to minimize clearances between the case and the rotating turbine blades. For the abradability rig testing, rectangular coupons were used for coating development as shown in Fig. 25(a). Three 25.4 mm diameter circular coupons were also attached for metallography and thermal cycling. Three sets of microstructures were generated with a denser bottom layer of $\sim$ 25% porosity and porous top layer with porosity values of 45, 35 and 25%. During the spray, backside temperature of the samples was monitored using a welded
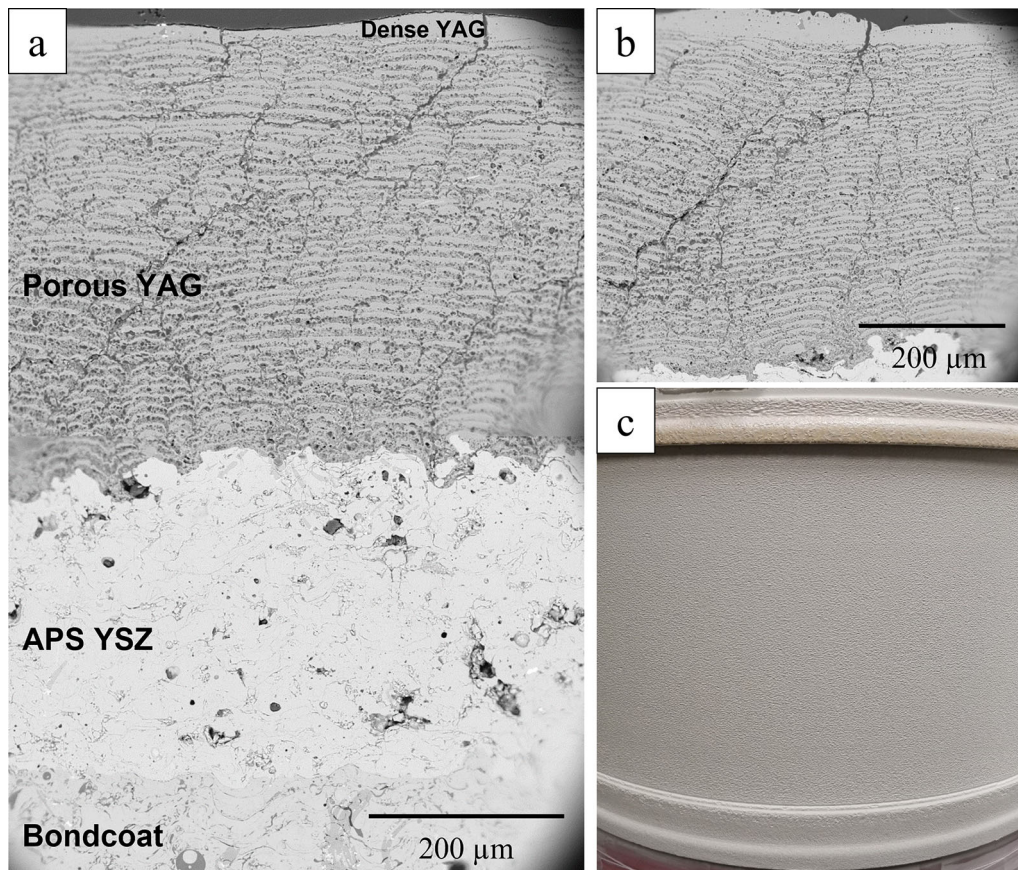
Fig. 24 Titan 250 liner coated with SPPS YAG. (a) Microstructure of the entire TBC, (b) magnified image of SPPS YAG layer and, (c) titan 250 liner after coating

thermocouple. A sample temperature profile is shown in Fig. 25(b), where higher backside temperature was maintained for the dense layer and a cooler temperature was maintained for the porous layer. Stoppage time between the coating passes were also controlled to allow sufficient cooling of the samples before the start of the next pass. The porosity of the coating was controlled by changing the standoff distance and a variation of 15 mm was used to alter the coating porosity from 25-45%. The microstructures obtained are shown in Fig. 26 where (a) and (b) have a top layer with 44% and 36% porosity respectively and a bottom layer with 23% and 24% porosity respectively. The last microstructure is one layered and has an overall porosity of 26%. The abradability rig test conditions and the results are summarized in Part II of this paper and indicate there is a preferred porosity level. All test samples exceeded the 100 ten-hour thermal cycle at 1150 °C requirement (1200 h) and had sufficient durability for the application.

Generation of Coatings for Turbine Ceramic Outer Air Seals

Based on the results from abradability rig testing described in Part II of this paper, a single layered YAG microstructure with 28% porosity was down selected for application on air seals. SPPS.

YAG target thickness of 0.5, 1 and 1.5 mm were to be deposited depending on the tip shoe location. The air seal parts had a concave geometry with a 41 cm radius of curvature. Thus, initial fixturing involved attaching four air seal scrap parts on a turntable and spun around the respective radius. As only four samples were attached simultaneously on an 82 mm diameter, samples only comprised of ∼ 20% of the entire spray area leading to enormous precursor waste and longer spray times. Instead, the spray setup was switched from rotation to moving the robot back and forth on the base axis using joint control commands to obtain an accurate fixed radius for the gun path to achieve accurate standoff distance control. During the spray event, as the thickness of the coatings increased over 500 microns, edge chipping was observed. To prevent this, a new fixture was designed as shown in Fig. 27a.

Fig. 25 (a) Spray setup for coating abradability testing samples and (b) backside temperature measurement during spray process to control coating porosity
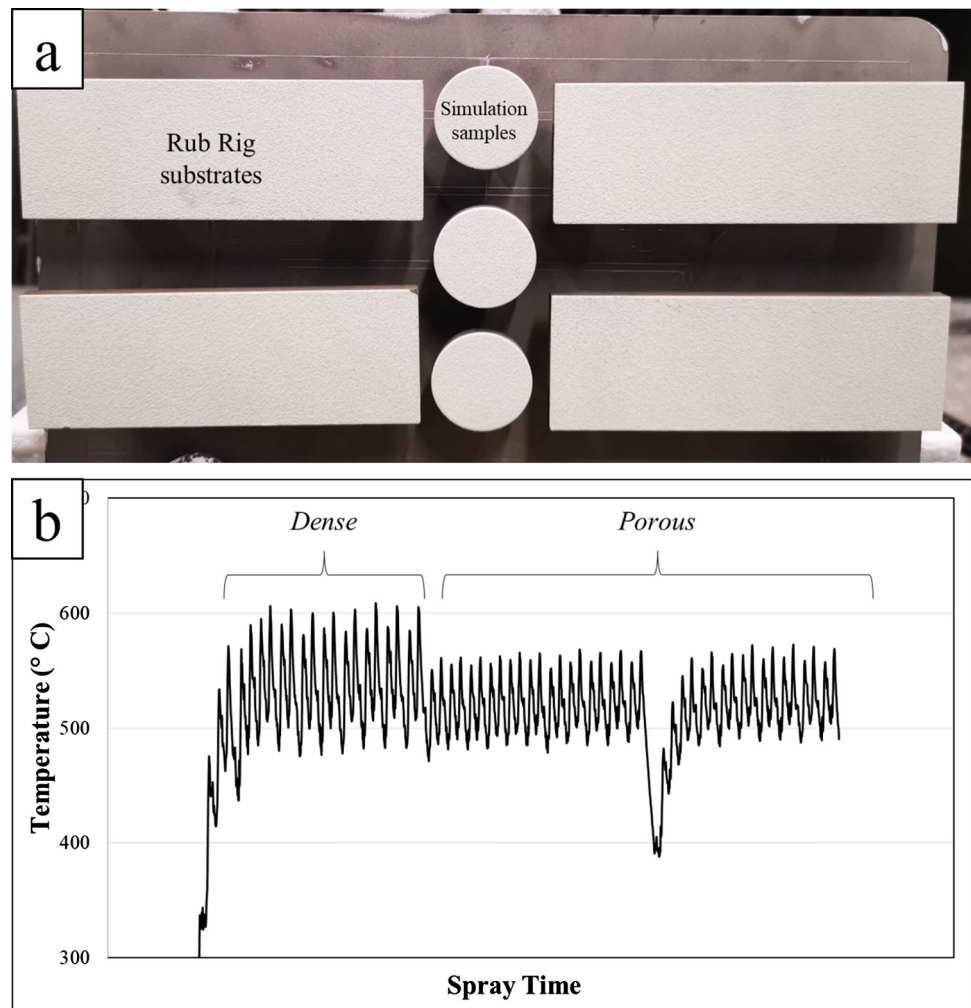
Chipping was reduced, and coating deposition on the part edges was improved. Using the setup, coatings were applied across the thickness range of 0.5-1.5 mm on parts and the microstructures are shown in Fig. 28. All three microstructures have a porosity of $\sim$ 25%.

Conclusions

SPPS YAG coatings were successfully developed using a high enthalpy Sinplex plasma gun with comparable microstructures to the ones developed with the 9 MB gun in a previous study. Sinplex Pro benefits are significantly higher deposition rate, upto 382 g/hr. as compared to 9 MB with a maximum deposition rate of 139 g/hr. (Ref 26) for YAG-based coatings, and 2X higher standoff distance. Using Taguchi design of experiments, porous coatings were developed with ultra-low thermal conductivity (0.48 W/mK) and high deposition rates (382 g/hour). Similarly, extremely dense coatings ($\sim$ 10% porosity) were developed that exhibited greater erosion resistance than baseline

APS YSZ. Using the knowledge of making porous and dense microstructures, coatings with a graded porosity were developed which were later successfully applied to engine parts. The process properties relationships developed allowed the production of different coating microstructures needed for the different engine parts.

A two layered coating with a thick porous inner layer and a thin dense outer layer was applied to annular combustor liner. Two-layered coatings with a dense bottom layer and a porous top layer were generated for abradability rig testing. Using the results from the test, thick SPPS YAG coatings (0.5 -15 mm) were successfully applied on turbine outer air seal components. This work has demonstrated the flexibility of the SPPS process to generate a variety of microstructures needed for various engine components and for the first time defined the process for spraying durable coatings on engine components.

Part II of this paper describes the technology transfer process to Solar, their successful coating of rig and engine components and the property improvements demonstrated.
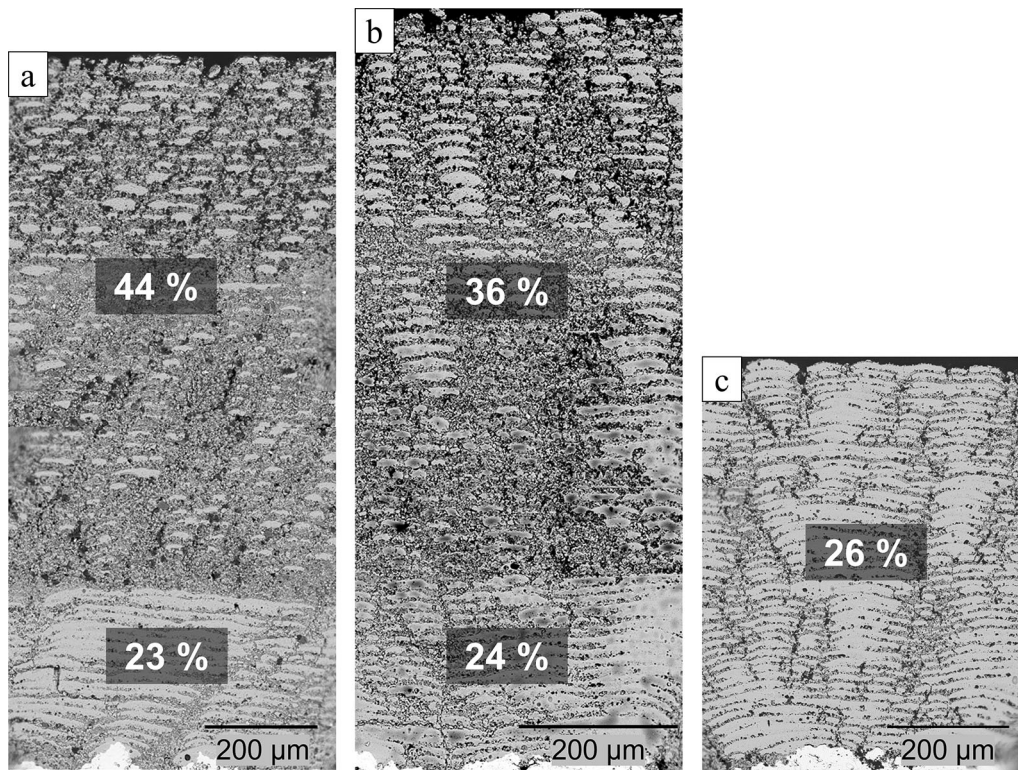
Fig. 26 SPPS YAG microstructures for abradability testing with varying porosity
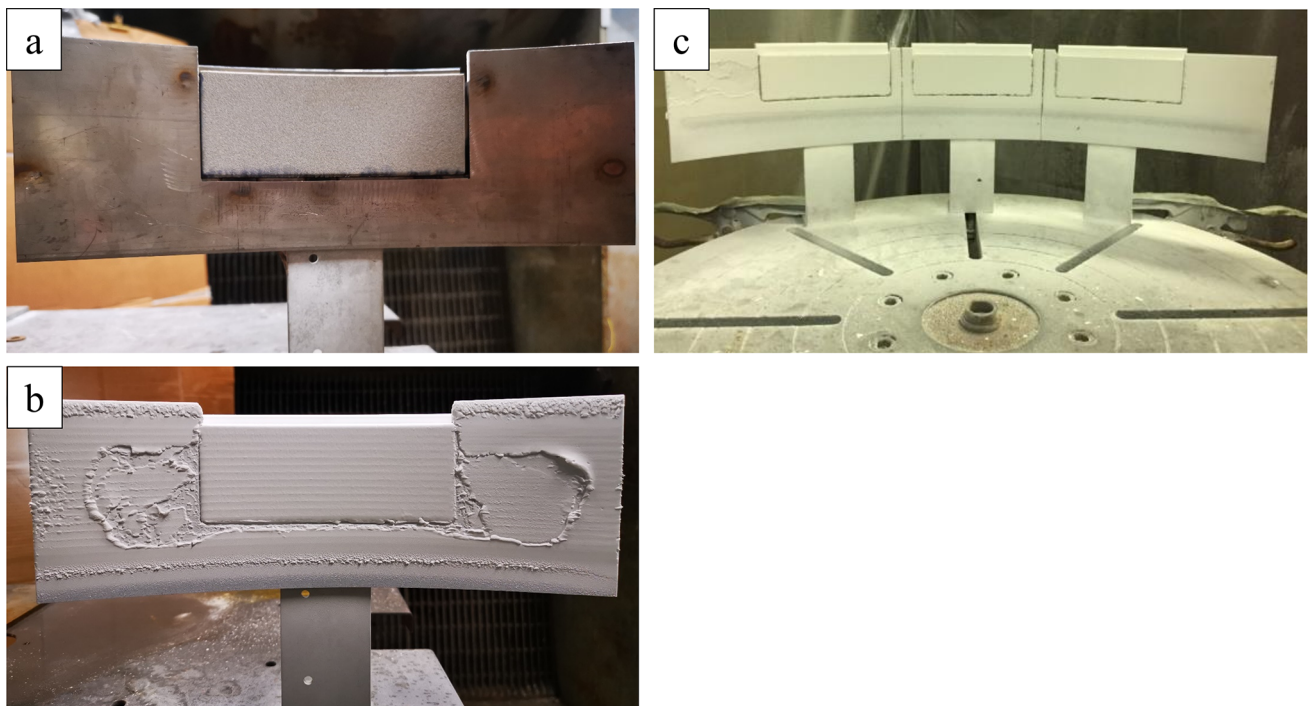

Fig. 27 Fixture for coating air seals which reduced coating chipping along part perimeter. Single air seal fixtures initially developed at SST (a-uncoated and b-coated) that resulted in the development of a fixture for multiple parts coated at Solar (c)
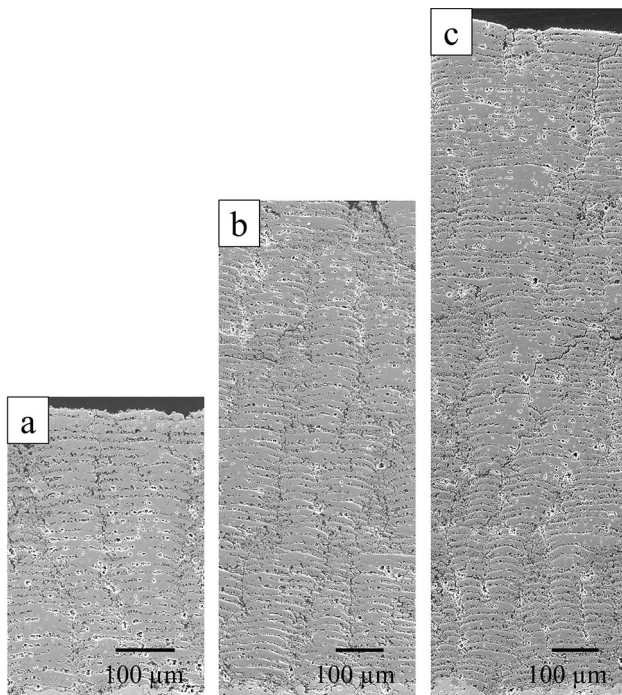
Fig. 28 Microstructures of SPPS YAG coatings with (a) 0.5 mm, (b) 1 mm and (c) 1.5 mm thick YAG

References

1. N.P. Padture, M. Gell and E.H. Jordan, Thermal Barrier Coatings for Gas-Turbine Engine Applications, *Science (80-.)*, 2002, **296**(5566), p 280-284. https://doi.org/10.1126/science.1068609

2. M.J. Stiger, N.M. Yanar, M.G. Topping, F.S. Pettit and G.H. Meier, Thermal Barrier Coatings for the 21st Century, *Zeitschrift fur Met.*, 1999, **90**, p 1069-1078.

3. R.A. Miller, Thermal Barrier Coatings for Aircraft Engines: History and Directions, *J. Therm. Spray Technol.*, 1995, **6**(1), p 35-42.

4. A.G. Evans, D.R. Mumm, J.W. Hutchinson, G.H. Meier and F.S. Pettit, Mechanisms Controlling the Durability of Thermal Barrier Coatings, *Prog. Mater. Sci.*, 2001, **46**(5), p 505-553. https://doi.org/10.1016/S0079-6425(00)00020-7

5. D.R. Clarke, M. Oechsner and N.P. Padture, Thermal-Barrier Coatings for More Efficient Gas-Turbine Engines, *MRS Bull.*, 2012, **37**(10), p 891-898.

6. J.H. Perepezko, The Hotter the Engine, the Better, *Science (80-.)*, 2009, **326**, p 1068-1069.

7. C. Mercer, J.R. Williams, D.R. Clarke and A.G. Evans, On a Ferroelastic Mechanism Governing the Toughness of Metastable Tetragonal-Prime (T′) Yttria-Stabilized Zirconia, *Proc. R. Soc. Lond. A Math. Phys. Eng. Sci.*, 2007, **463**, p 1393-1408.

8. X.Q. Cao, R. Vassen and D. Stoever, Ceramic Materials for Thermal Barrier Coatings, *J. Eur. Ceram. Soc.*, 2004, **24**(1), p 1-10. https://doi.org/10.1016/S0955-2219(03)00129-8

9. R.A. Miller, J.L. Smialek, R.G. Garlick, Phase Stability in Plasma Sprayed Partially Stabilized Zirconia-Yttria, in *Advances in Ceramics. Volume 3, Science and Technology of Zirconia*, 1981, p 242-253.

10. R. Vassen, A. Stuke and D. Stöver, Recent Developments in the Field of Thermal Barrier Coatings, *J. Therm. Spray Technol.*, 2009, **18**(2), p 181-186. https://doi.org/10.1007/s11666-009-9312-7

11. L. Li, N. Hitchman and J. Knapp, Failure of Thermal Barrier Coatings Subjected to CMAS Attack, *J. Therm. Spray Technol.*, 2010, **19**(1-2), p 148-155. https://doi.org/10.1007/s11666-009-9356-8

12. M.P. Borom, C.A. Johnson and L.A. Peluso, Role of Environment Deposits and Operating Surface Temperature in Spallation of Air Plasma Sprayed Thermal Barrier Coatings, *Surf. Coatings Technol.*, 1996, **86**, p 116-126.

13. D.R. Clarke and S.R. Phillpot, Thermal Barrier Coating Materials, *Mater. Today*, 2005, **8**(6), p 22-29. https://doi.org/10.1016/S1369-7021(05)70934-2

14. C.G. Levi, Emerging Materials and Processes for Thermal Barrier Systems, *Curr. Opin. Solid State Mater. Sci.*, 2004, **8**(1), p 77-91.

15. D. Stöver, G. Pracht, H. Lehmann, M. Dietrich, J.-E. Döring and R. Vaßen, New Material Concepts for the Next Generation of Plasma-Sprayed Thermal Barrier Coatings, *J. Therm. Spray Technol.*, 2004, **13**(1), p 76-83. https://doi.org/10.1361/10599630418176

16. S. Ghosh, Thermal Barrier Ceramic Coatings—A Review, in *Advanced Ceramic Processing*, 2015, p 75-100, https://doi.org/10.5772/61346.

17. R.L. Jones, R.F. Reidy and D. Mess, Scandia, Yttria-Stabilized Zirconia for Thermal Barrier Coatings, *Surf. Coatings Technol.*, 1996, **82**(1-2), p 70-76.

18. D.-J. Kim, Effect of Ta_2O_5, Nb_2O_5, and HfO_2 Alloying on the Transformability of Y_2O_3-Stabilized Tetragonal ZrO_2, *J. Am. Ceram. Soc.*, 1990, **73**(1), p 115-120.

19. D. Zhu and R.A. Miller, Sintering and Creep Behavior of Plasma-Sprayed Zirconia-and Hafnia-Based Thermal Barrier Coatings, *Surf. Coatings Technol.*, 1998, **108109**, p 114-120.

20. F.M. Pitek and C.G. Levi, Opportunities for TBCs in the ZrO_2-$YO_{1.5}$-$TaO_{2.5}$ system, *Surf. Coatings Technol.*, 2007, **201**(12), p 6044-6050.

21. W. Ma, D. Mack, J. Malzbender, R. Vaßen and D. Stöver, Yb_2O_3 and Gd_2O_3 Doped Strontium Zirconate for Thermal Barrier Coatings, *J. Eur. Ceram. Soc.*, 2008, **28**(16), p 3071-3081. https://doi.org/10.1016/j.jeurceramsoc.2008.05.013

22. M.O. Jarligo, G. Mauer, D. Sebold, D.E. Mack, R. Vaßen and D. Stöver, Decomposition of $Ba(Mg_{1/3}Ta_{2/3})O_3$ Perovskite during Atmospheric Plasma Spraying, *Surf. Coatings Technol.*, 2012, **206**(8-9), p 2515-2520. https://doi.org/10.1016/j.surfcoat.2011.11.003

23. M. Gell, J. Wang, R. Kumar, J. Roth, C. Jiang and E.H. Jordan, Higher Temperature Thermal Barrier Coatings with the Combined Use of Yttrium Aluminum Garnet and the Solution Precursor Plasma Spray Process, *J. Therm. Spray Technol.*, 2018, **27**, p 543-555. https://doi.org/10.1007/s11666-018-0701-7

24. R. Kumar, E.H. Jordan, M. Gell, J. Roth, C. Jiang, J. Wang and S. Rommel, CMAS Behavior of Yttrium Aluminum Garnet (YAG) and Yttria-Stabilized Zirconia (YSZ) Thermal Barrier Coatings, *Surf. Coat. Technol.*, 2017, **327**, p 126-138.

25. E.H. Jordan, M. Gell, C. Jiang, J. Wang, B. Nair, High Temperature Thermal Barrier Coating Made by the Solution Precursor Plasma Spray Process, in *Proceedings of the ASME Turbo Expo: Turbine Technical Conference and Exposition*, **6**, 2014, p V006T02A007. https://doi.org/10.1115/GT2014-26254.

26. R. Kumar, J. Wang, C. Jiang, D. Cietek, J. Favata, S. Shahbazmohamadi, J. Roth, M. Gell and E.H. Jordan, Low Thermal

Conductivity Yttrium Aluminum Garnet Thermal Barrier Coatings Made by the Solution Precursor Plasma Spray: Part I—Processing and Properties, *J. Therm. Spray Technol.*, 2018, **27**(5), p 781-793. https://doi.org/10.1007/s11666-018-0728-9

27. R. Kumar, C. Jiang, J. Wang, D. Cietek, J. Roth, M. Gell and E.H. Jordan, Low Thermal Conductivity Yttrium Aluminum Garnet Thermal Barrier Coatings Made by the Solution Precursor Plasma Spray: Part II—Planar Pore Formation and CMAS Resistance, *J. Therm. Spray Technol.*, 2018, **27**(5), p 794-808. https://doi.org/10.1007/s11666-018-0727-x

28. O. Fabrichnaya, S. Lakiza, C. Wang, M. Zinkevich, C.G. Levi and F. Aldinger, Thermodynamic Database for the ZrO_2-$YO_{3/2}$-$GdO_{3/2}$-$AlO_{3/2}$ System and Application to Thermal Barrier Coatings, *J. Phase Equilibria Diffus.*, 2006, **27**(4), p 343-352.

29. R. Vassen, X.X. Cao, F. Tietz, D. Basu, D. Stover and D. Stöver, Zirconates as New Materials for Thermal Barrier Coatings, *J. Am. Ceram. Soc.*, 2004, **83**(8), p 2023-2028. https://doi.org/10.1111/j.1151-2916.2000.tb01506.x

30. G. Suresh, G. Seenivasan, M. Krishnaiah and P.S. Murti, Investigation of the Thermal Conductivity of Selected Compounds of Lanthanum, Samarium and Europium, *J. Alloys Compd.*, 1998, **269**(1-2), p L9-L12.

31. R. Kumar, D. Cietek, C. Jiang, J. Roth, M. Gell and E.H. Jordan, Influence of Microstructure on the Durability of Gadolinium Zirconate Thermal Barrier Coatings Using APS & SPPS Processes, *Surf. Coat. Technol.*, 2018, **337**(C), p 117-125. https://doi.org/10.1016/j.surfcoat.2018.01.004

32. M. Gell, E.H. Jordan, M. Teicholz, B.M. Cetegen, N.P. Padture, L. Xie, D. Chen, X. Ma and J. Roth, Thermal Barrier Coatings Made by the Solution Precursor Plasma Spray Process, *J. Therm. Spray Technol.*, 2008, **17**, p 124-135.

33. E.H. Jordan, C. Jiang and M. Gell, The Solution Precursor Plasma Spray (SPPS) Process: A Review with Energy Considerations, *J. Therm. Spray Technol.*, 2015, **24**(7), p 1153-1165. https://doi.org/10.1007/s11666-015-0272-9

34. A. Jadhav, N.P. Padture, F. Wu, E.H. Jordan and M. Gell, Thick Ceramic Thermal Barrier Coatings with High Durability Deposited Using Solution-Precursor Plasma Spray, *Mater. Sci. Eng. A*, 2005, **405**, p 313-320. https://doi.org/10.1016/j.msea.2005.06.023

35. L. Pawlowski, Suspension and Solution Thermal Spray Coatings, *Surf. Coat. Technol.*, 2009, **203**, p 2807-2829.

36. L. Xie, X. Ma, E.H. Jordan, N.P. Padture, D.T. Xiao and M. Gell, Deposition Mechanisms of Thermal Barrier Coatings in the Solution Precursor Plasma Spray Process, *Surf. Coatings Technol.*, 2004, **177-178**, p 103-107.

37. R. Kumar, S. Rommel, C. Jiang and E.H. Jordan, Effect of CMAS Viscosity on the Infiltration Depth in Thermal Barrier Coatings of Different Microstructures, *Surf. Coatings Technol.*, 2021, **432**, 128039. https://doi.org/10.1016/j.surfcoat.2021.128039

38. Up To 400% Efficiency Gain Without Compromise « Oerlikon Metco, n.d., https://www.oerlikon.com/metco/en/products-services/coating-equipment/thermal-spray/spray-guns/cascading-arc-landing-page/. Accessed 16 March 2018.

39. SinplexPro Plasma Spray Gun « OerlikonMetco,n.d., https://www.oerlikon.com/metco/en/products-services/coating-equipment/thermal-spray/spray-guns/coating-equipment-plasma/sinplexpro/. Accessed 16 March 2018.

40. A. Vardelle, C. Moreau, J. Akedo, H. Ashrafizadeh, C.C. Berndt, J.O. Berghaus, M. Boulos, J. Brogan, A.C. Bourtsalas, A. Dolatabadi, M. Dorfman, T.J. Eden, P. Fauchais, G. Fisher, F. Gaertner, M. Gindrat, R. Henne, M. Hyland, E. Irissou, E.H. Jordan, K.A. Khor, A. Killinger, Y.-C. Lau, C.-J. Li, L. Li, J. Longtin, N. Markocsan, P.J. Masset, J. Matejicek, G. Mauer et al., The 2016 Thermal Spray Roadmap, *J. Therm. Spray Technol.*, 2016, **25**(8), p 1376-1440. https://doi.org/10.1007/s11666-016-0473-x

41. E.H. Jordan, C. Jiang, J. Roth and M. Gell, Low Thermal Conductivity Yttria-Stabilized Zirconia Thermal Barrier Coatings Using the Solution Precursor Plasma Spray Process, *J. Therm. Spray Technol.*, 2014, **23**, p 849-859.

42. V. Viswanathan, G. Dwivedi and S. Sampath, Engineered Multilayer Thermal Barrier Coatings for Enhanced Durability and Functional Performance, *J. Am. Ceram. Soc.*, 2014, **97**(9), p 2770-2778. https://doi.org/10.1111/jace.13033